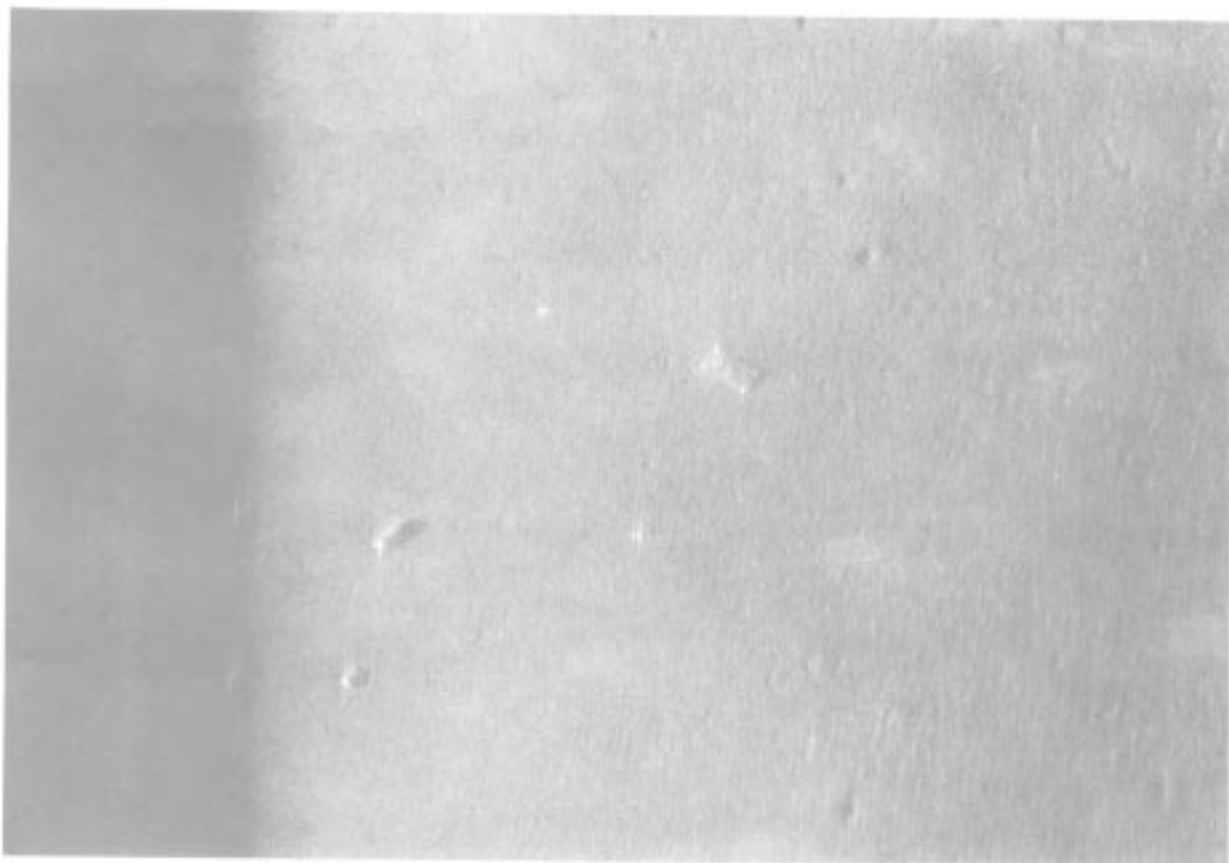


Naval Research Reviews

Office of Naval Research
Three/1997
Vol XLIX



Remote Minehunting



An image of the target field using the high frequency synthetic aperture sonar. The sonar is 25 feet above the bottom and the water depth is 98 feet. The maximum range displayed in the image is approximately 250 feet. In the near ranges, a number of cylindrical targets of varying sizes and orientations are clearly visible, as are their shadows. Also evident are the images of two spheres which appear as a pair of bright dots.

Naval Research Reviews

Office of Naval Research
Three/1997
Vol XLIX

Articles

2

Foreword

Douglas Todoroff, Guest Editor

3

High Frequency/Low Frequency Synthetic Aperture Sonar

*Gary S. Sammelmann, Jose E.
Fernandez, James T. Christoff, Leonid
Vaizer, John D. Lathrop, Robert W. Sheriff
& Thomas C. Montgomery*

9

Automated Detection/ Classification of Sea Mines in Sonar Imagery

*Gerald J. Dobeck, John C. Hyland
& Le'Derick Smedley*

21

Underwater Electro- Optical System for Mine Identification

Michael P. Strand

29

Advances in the Magnetic Detection and Classification of Sea Mines and Unexploded Ordnance

Ted R. Clem



CHIEF OF NAVAL RESEARCH

RADM Paul G. Gaffney, II, USN

DEPUTY CHIEF OF NAVAL RESEARCH
TECHNICAL DIRECTOR

Dr. Fred Saalfeld

CHIEF WRITER/EDITOR

William J. Lescure

SCIENTIFIC EDITOR

Douglas Todoroff

MANAGING EDITOR

Norma Gerbozy

ART DIRECTION

*Cynthia Nishikawa
Jorge Scientific Corporation*

Departments

46

Profiles in Science

47

Research Notes

About the cover

The Dolphin Towed Advanced Sensor was used to detect, classify, and identify mine threats from deep to shallow water. Camera good-luck caught a real dolphin near its mechanical namesake. The sensor is a semi-autonomous vehicle, towed by a remotely controlled semi-submersible. It is a prototype and this experiment was proof of the concept only, not of the hardware.

Naval Research Reviews publishes articles about research conducted by the laboratories and contractors of the Office of Naval Research and describes important naval experimental activities. Manuscripts submitted for publication, correspondence concerning prospective articles, and changes of address, should be directed to Code 00PA, Office Naval Research, Arlington, VA 22217-5660. Requests for subscriptions should be directed to the Superintendent of Documents, U.S. Government Printing Office, Washington, DC 20403. *Naval Research Reviews* is published from appropriated funds by authority of the Office of Naval Research in accordance with Navy Publications and Printing Regulations. NAVSOP-35.

Foreword

*Douglas Todoroff, Guest Editor
Office of Naval Research*

In the post-Cold War environment, naval warfare priorities have shifted from open/blue-water-basin operations to regional, shallow water Third World conflicts as the major technology challenges facing naval operations in the 21st century. This increased importance of responding to littoral conflicts has highlighted the demanding requirements for developing effective sea-mine countermeasures in shallow and very shallow water. Thus, it is appropriate at this time that the *Naval Research Reviews* should devote a theme issue to the critical problem of countering the mine threat. In this issue, we focus on recent technology developments in the area of mine detection, classification and identification.

The recent interest in mine countermeasures is a result of the proliferation of mines and the threat they pose to naval operations. Mines can be easily obtained and used by any nation. Sophisticated mines can now be purchased commercially, and crude copies of sophisticated mines can be manufactured in-house, even by those nations with limited industrial capabilities. As a result, mines have become a weapon of choice for Third World countries. Mines have been used repeatedly in the last quarter century to threaten commercial shipping, to cover aggressive actions, and to attack naval vessels. In recent years, USS Roberts, USS Tripoli, and USS Princeton have all been victims of naval mining.

The diversity of mines available to regional powers makes shallow water mine countermeasures perhaps the most technology challenging of all naval mission requirements. In deep water, tethered mines constitute the main threat to naval operations. In shallow water, however, the mine threat consists of bottom, volume, and floating mines. Here shallow water refers to depths less than 100 meters. A very shallow water regime has been defined as the coastal region with water depths from 11 to 3 meters. In this regime, the threat consists primarily of bottom-influence sea mines, smaller anti-invasion mines, moored mines, and floating mines. Additionally, the likelihood of mine burial increases as the water depth decreases.

As a result, there is no single, simple solution to the mine detection problem. In particular, it is generally recognized that pure acoustic approaches to the detection of underwater sea mines cannot be as effective as multidisciplinary techniques. In this issue, we include recent mine detection technology advances in both acoustics and non-acoustics.

The first article is by researchers at Coastal Systems Station (NSWC) and Northrup Grumman regarding recent developments in synthetic aperture sonar for mine detection and classification. Synthetic aperture sonar, like synthetic aperture radar, involves the processing of data from a small

physical aperture to provide high resolution imagery. In this article, a description of a novel motion compensation technique is presented which is critical to the application of synthetic aperture sonar technology for minehunting.

In the second article, Dobeck, et.al. describe an approach to automated detection and classification of sea mines in sonar imagery which has performance similar to that of an expert sonar operator. Their approach utilizes an improved detection density algorithm, a feature extraction technique that uses a stepwise feature selection strategy, and two independent classifiers. In this article, the authors demonstrate significant improvement in overall classification by "ANDING" classifiers which use complementary statistical, mathematical, and geometrical constructs to describe class boundaries in feature space.

The third article address the identification of proud, partially buried, and moored mines in shallow and very shallow water. Mine identification is a critical phase of minehunting in which mines are discriminated from mine like contacts prior to neutralization. In this article, Mike Strand describes a comparison of laser range-gated and laser line scan technologies for mine identification.

The final article describes recent advances in the magnetic detection and classification of sea mines and of unexploded ordnance. In this article, Ted Clem describes the development of a 5-channel tensor magnetic gradiometer that provides significant improvements in classification and localization over that offered by the commonly used single-channel total field magnetometer. While the current configuration of this sensor features bulk niobium low critical temperature superconducting components, recent advances in material research will allow development of a high temperature superconducting gradiometer concept using liquid nitrogen refrigerant to reduce package size and cryogenic support requirements.

The technologies described in this issue of *Naval Research Reviews* represent significant advances in the detection, classification, and identification of sea mines. The synthetic aperture sonar, automated processing, and electro-optic identification technologies will be demonstrated to the operational user as part of the Joint Countermine Advanced Concept Technology Demonstration (ACTD) in fiscal year 1998.

High Frequency/Low Frequency Synthetic Aperture Sonar

*Gary S. Sammelmann, Jose E. Fernandez, James T. Christoff, Leonid Vaizer, & John D. Lathrop
Coastal Systems Station, Dahlgren Division, Naval Surface Warfare Center, Panama City FL*

*Robert W. Sheriff & Thomas C. Montgomery
Northrop Grumman, Oceanic Division, Annapolis MD*

Abstract

The HF/LF SAS (high frequency/low frequency SAS) is a high resolution SAS developed by COASTSYSTA and Northrop Grumman for the shallow water (SW) and very shallow water (VSW) regimes. This sonar suite has recently been delivered to COASTSYSTA and it is currently undergoing field testing. This article describes this sonar and the type of resolution and acoustical images which are expected from this sonar. The application of this sonar to the SW and VSW regimes required the development of a novel method of motion compensation. A description of this method and the type of accuracy's expected from this technique are presented. Finally, a look at future broad band systems and their predicted performance is presented.

1. Introduction

The HF/LF SAS (high frequency / low frequency synthetic aperture sonar) is a high resolution synthetic aperture sonar developed by COASTSYSTA and Northrop Grumman to detect, classify, and identify mine-like targets in the shallow water (SW) and very shallow water (VSW) regimes. The LFSAS is expected to be able to detect and classify volume, proud, and buried mines with its 3"x3" resolution. The HFSAS with its 1"x1" resolution is expected to have an identification capability approaching that of some optical systems.

The HF/LF SAS was delivered to COASTSYSTA in July of 1996, and it is currently undergoing field testing. This article describes the design and the type of performance ex-

pected from the HF/LF SAS. This article also describes the novel motion compensation technique developed by COASTSYSTA and Northrop Grumman for this sensor.

Section 2 of this article describes the design of the HF/LF SAS, and Section 3 describes the motion compensation algorithms. Section 4 describes the current performance of the HF/LF SAS.

2. Hardware Design

The main design objective of HF/LF SAS was to design a small, light weight, high resolution acoustic sensor for operation in the SW and VSW regimes which was compatible with operation in a UUV (unmanned underwater vehicle). Compatibility requirements with MK 48 based UUVs constrained the dimensions of this sensor to a cylindrical body 21 inches in diameter in a section no longer than 36 inches. The requirement that the sensor be able to detect, classify, and identify mine-like targets and fit within the above section can only be satisfied by a SAS. The requirement that it be able to detect and classify buried targets, and identify volume and proud targets suggested a dual frequency approach consisting of a low frequency SAS similar to MADOM to detect and classify buried targets, and a high frequency SAS for identification of volume and proud targets. The horizontal and vertical beam widths of the sensor and the depression angle of the sensor have been optimized

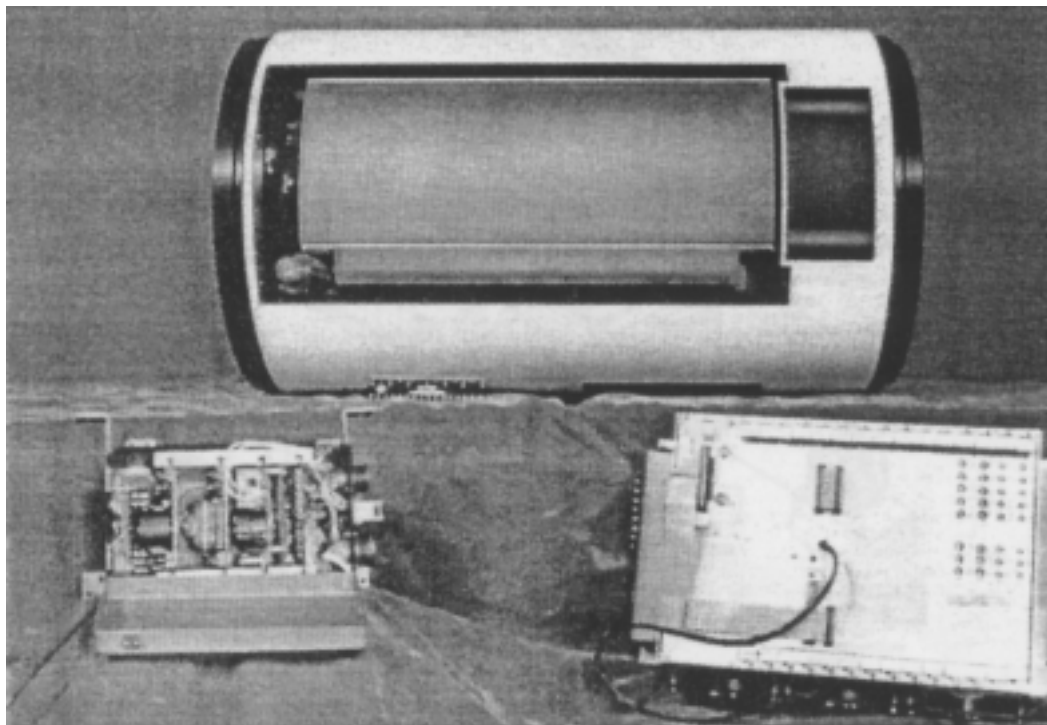
to produce the greatest signal-to-noise ratio (SNR) and coverage in the shallow and very shallow water environment using PC SWAT. The length of the receiver was chosen to attain the desired maximum range at a given platform velocity.

Past experience with MADOM showed that a LFSAS with a central frequency of 20 kHz and band width of 10 kHz was capable of detecting and classifying buried targets. As a proof of concept, the original MADOM configuration was modified to have a central frequency of 20 kHz with a 10 kHz band width and 6 inch elements. This configuration gave MADOM the capability of achieving 3"x3" resolution. In December 1992, a trial sea test of this configuration demonstrated the concept. The concept was further demonstrated in September 1995 at the MUDSS (Mobile Underwater Survey System) Feasibility Demonstration, where this modified version of MADOM successfully detected and classified targets ranging in size from a 60 millimeter howitzer shell to a 2000 lb. bomb. During this demonstration, the HPSS (High Performance Sidescan Sonar) was employed in a SAS configuration as a HFSAS. However, due to problems with the filters, this sonar was only able to achieve 5 cm x 15 cm resolution.

The major obstacle inhibiting performance of the LF/HF SAS was the motion of the sensor away from a straight line trajectory. The method of overcoming this problem was to develop an adaptive motion compensation technique which determines the ping to ping motion of the vehicle based on

Figure 1

Photograph of the completed system.



the correlation between elements of neighboring pings. The method chosen for this motion compensation was a technique whereby the last 2 phase centers of the array overlap with the first 2 phase centers of the next ping. The time delay estimates between these overlapping pairs of phase centers allows one to determine the translation, pitch, and yaw motion of the array between adjacent pings. For this purpose, the array was designed with an extra pair of elements in order to facilitate the necessary 2 phase center overlap between adjacent pings and reduce the magnitude of the grating lobes of the array.

To facilitate the motion compensation estimates of the array, a Motion Measurement Package (MMP) consisting of a Doppler sonar, and an Inertial Navigation System (INS) was included. The INS allows one to determine an approximate value of the motion of the sensor. However, the accuracy of INS is insufficient to achieve the desired resolution of the sensor. Hence, the need for an adaptive motion compensation technique, which has the potential of estimating the motion of the vehicle to within a thousandth of a wavelength, is necessary. However, the INS provides the operator with a baseline to compare the estimated motion with the motion measured by the INS. The Doppler sonar provides accurate velocity measurements. By slaving the ping repetition rate of the projector to the Doppler unit, one can reduce the effects of time varying velocity of the array along its trajectory, by requiring that the projector fire after the array has moved a predefined distance along track.

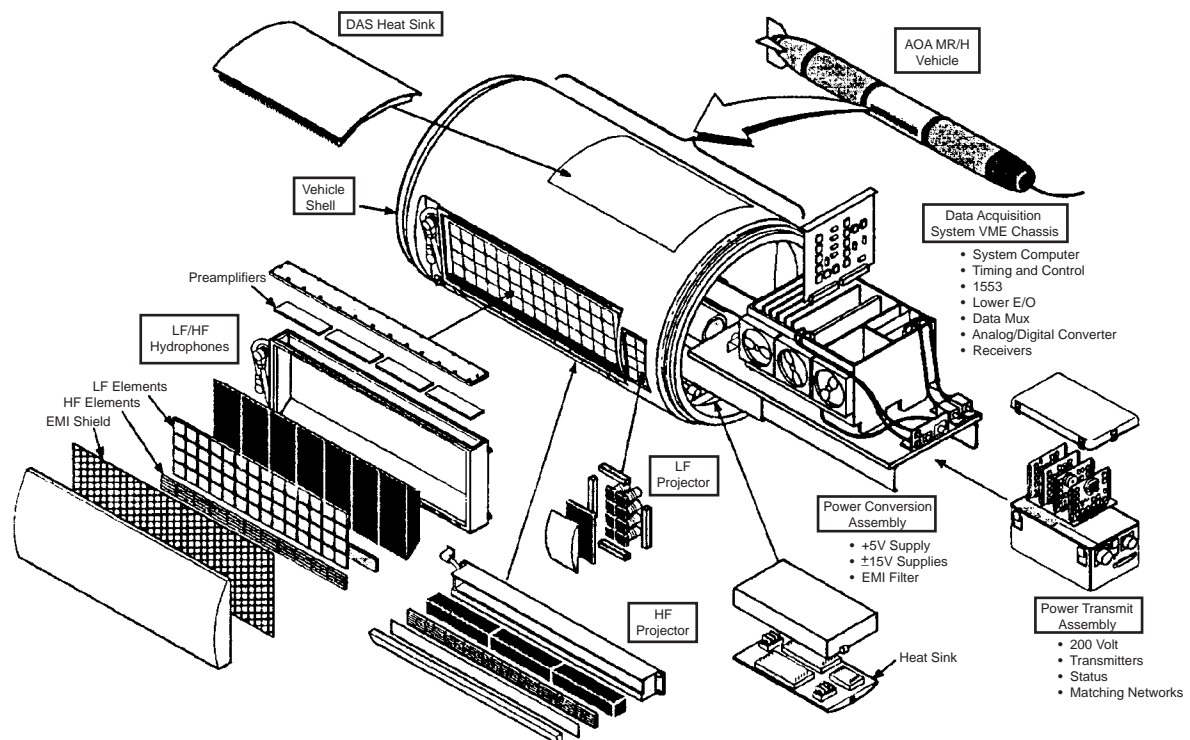
The projector of the LFSAS is a tonpilz design. The vertical height of the projector can be configured as either a one or two wavelength high projector by changing the jumper leads on the matching network assembly. The projector can produce a high fidelity 2 cycle CW pulse with a 10 kHz band width centered at 20 kHz.

The projector of the HFSAS is a standard half wavelength ceramic bar design. The projector consists of 10 elements in a linear array, which allows one to vary the center of the projector at will. The projector can produce a 6 cycle CW pulse with a 30 kHz bandwidth centered at 180 kHz.

The receive elements of the LFSAS and HFSAS have been designed using a PiezoRubber (PZR) as the active material. The LFSAS contains 14 elements with an element spacing of 1.5 inches. Only 12 of these 14 elements are used to form the synthetic beam. The remaining 2 are used to achieve the desired phase center overlap between adjacent pings. The HFSAS contains 11 elements with an element spacing of 2 inches. Only 9 of these 11 elements is used to form the synthetic beam. The remaining 2 are used to obtain the desired phase center overlap.

The number of elements in the LFSAS and HFSAS is determined by the maximum range (40 meters) of the sensor, and the maximum platform velocity (8 knots). The distance traveled between pings is 0.2286 meters or 9 inches. The LFSAS forms 3 beams with a spacing of 3 inches per ping, and the HFSAS forms 9 beams with a spacing of 1 inch per ping.

Figure 2
Exploded view of the 21 inch section.



A study of the predicted signal-to-noise ratio of the LFSAS and HFSAS as a function of depression angle showed that the signal to noise ratio for a proud target was maximized and the blind spot under the vehicle was minimized for a depression angle of 10 degrees.

Figure 1 shows a photograph of the completed system. Figure 2 shows an exploded view of the 21 inch section.

3. Motion Compensation

The method of motion compensation developed by Northrop Grumman and COASTSYSTA is an adaptive approach which utilizes the cross-correlation between elements of adjacent pings to estimate the time delay. This approach requires that the phase centers of the last 2 elements of a ping and the first 2 elements of the next ping overlap. Two overlapping elements are required to determine the ping-to-ping time delay and its rate of change.

The concept of using overlapped displaced phase centers (DPC) was first disclosed by R.S. Raven [1]. Subsequent work at Northrop Grumman and COASTSYSTA [2, 3] has demonstrated the ability of this technique to compensate for ping-to-ping translations and rotations.

The central idea to this motion compensation technique is the assumption that the signal from a pair of overlapping phase centers should be nearly identical, except for small deviations due to the motion of the platform. This assumption is based upon the notion that both phase centers are illuminating approximately the same footprint on the bottom, and have approximately the same travel time to any point on the bottom. However, contamination of the signal due to multipathing, and surface reverberation in particular, at the larger ranges tends to decrease the correlation between the two signals, since multipathing adds a time varying signal to the signal at the phase centers. Thus, one must compensate for the effect of multipathing at the larger ranges.

The second key assumption to this motion compensation technique is that the signals from the overlapping phase

Figure 3

Point response function of the HFSAS with no motion in the three cases: no motion compensation; one element overlap; and two element overlap.

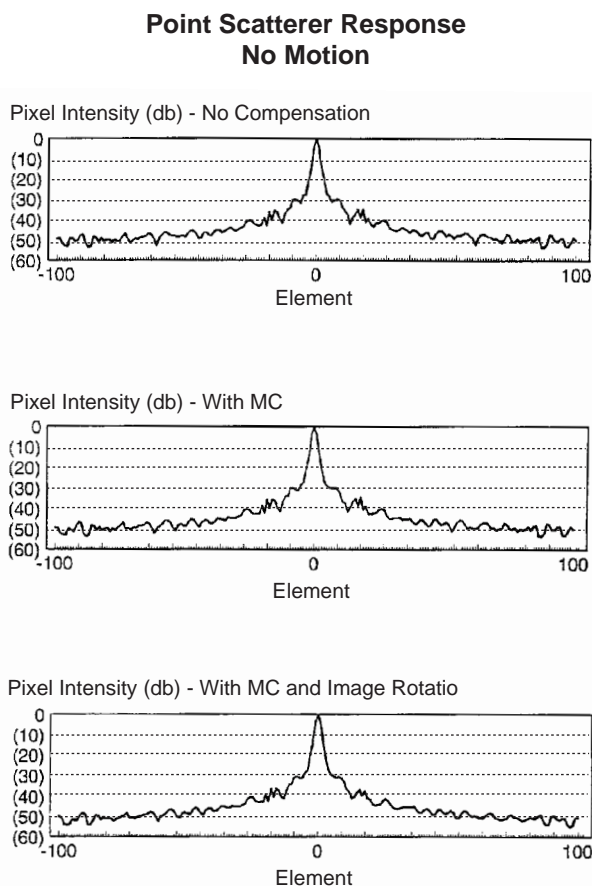
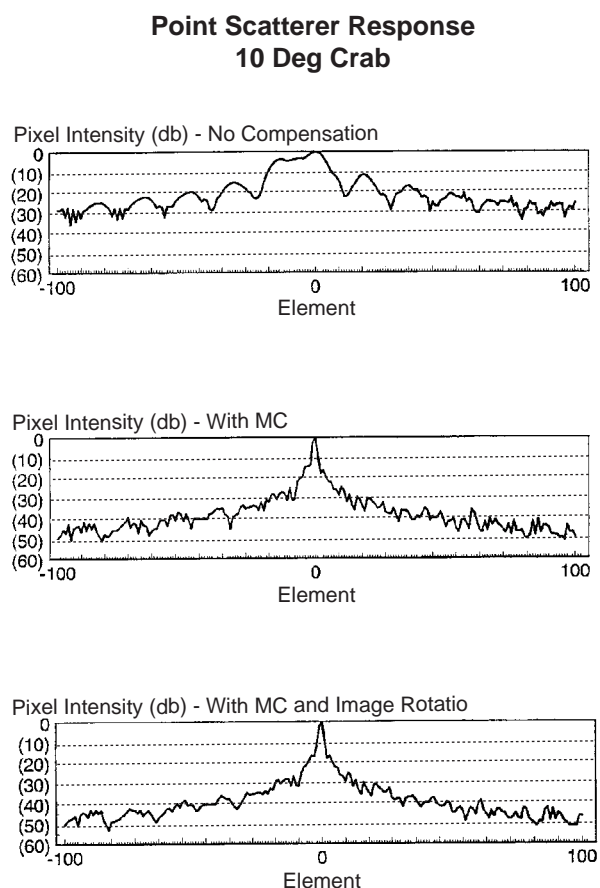


Figure 4

Point response function of the HFSAS with with a constant 10 degree crab in the three cases: no motion compensation; one element overlap; and two element overlap.



centers have a high correlation, and one can estimate the time delay between the two signals due to the motion of the platform by estimating the time delay in the cross correlation between these two signals. By using two overlapping phase centers, one can estimate the time delay and the rate of change of the time delay between two adjacent pings due to the motion of the platform.

Figure 3 shows the point response function of the HFSAS with no motion in the three cases: no motion compensation; one element overlap; and two element overlap. In all three cases, the point response function is close to its theoretical value.

Figure 4 shows the point response function with a constant 10 degree crab in the three cases: no motion compensation; one element overlap; and two element overlap. The case with no motion compensation is greatly distorted by the motion, whereas the two cases with motion compensation are similar to those without motion, indicating the motion compensation technique has properly removed the distortion of the synthetic beam pattern caused by the constant crab. This case shows that the case of one element overlap is sufficient to remove static time delays due to motion.

Figure 5
Point response function in the case of a sinusoidal yaw.

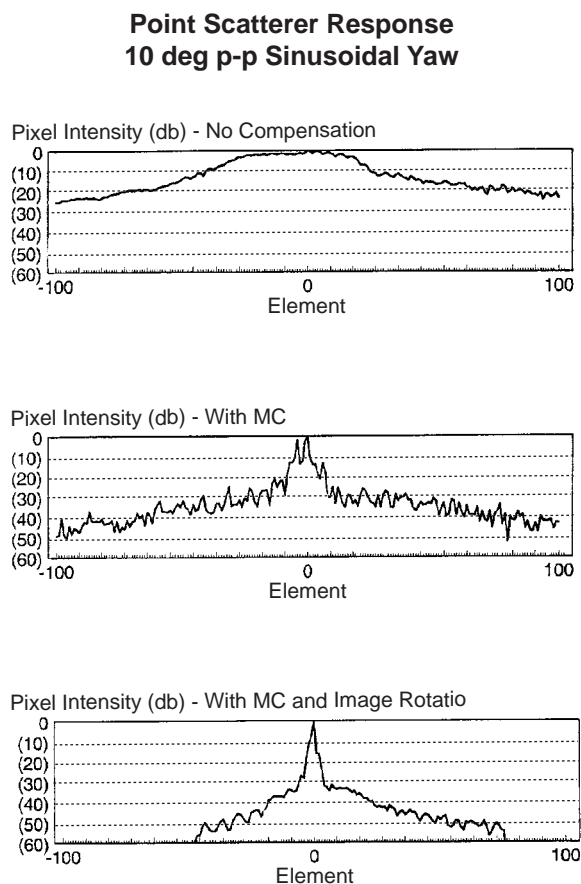


Figure 5 shows the point response function in the case of a sinusoidal yaw. The case with no motion compensation is greatly distorted by the yaw. The case with a one element overlap is somewhat distorted due to the time varying nature of the yaw.

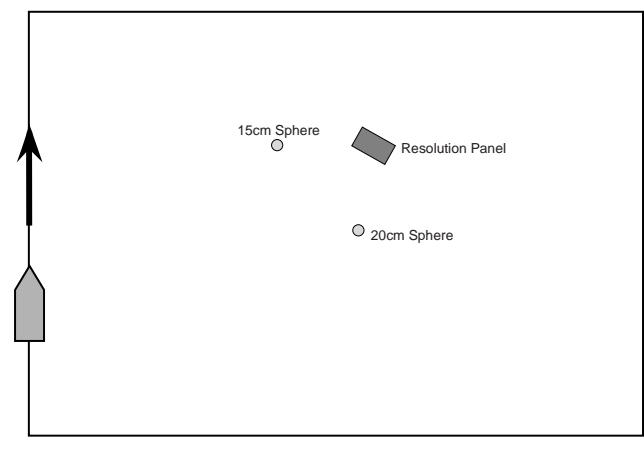
The case with a two element overlap is similar to the case with no motion indicating that the motion compensation technique with a two element overlap has correctly removed the distortion to the image due to the time varying yaw.

4. Performance

Figure 6 depicts an image of the target field during the sea tests of the HFSAS in the shallow water field.

The picture on the inside front cover of this issue depicts an image of the target field using the HFSAS. The image of 2 spheres and the resolution panel are clearly in evidence in this figure. The image of each sphere consists of 2 returns. The specular return, and a second return which may be an elastic return due to penetration of the fluid filled spheres. The legs of the resolution panel are clearly in evidence in this image, as are the doughnut shaped protrusions lying on the resolution panel.

Figure 6
Image of the target field using the HFSAS.



5. Conclusions

The recent completion of the HFSAS and LFSAS and the September 1996 sea test of this system offers new capabilities in mine detection, classification, and identification in shallow and very shallow water. The motion compensation technique described in this article holds the potential of predicting the time varying motion of the HFSAS and LFSAS

to a high degree of precision (a thousandth of a wavelength). During the next few months further refinements of this motion compensation technique will be worked out to refine the process and improve the quality of the HFSAS and LFSAS images.

Acknowledgments

The authors would like to acknowledge the support of Code 321 of the Office of Naval Research, with a special thanks to Dr. R. Jacobson, and Dr. W. Ching.

Biographies

Since 1984 Gary S. Sammelmann has been engaged in both theoretical and applied acoustics at the Coastal Systems Station. He is the coauthor of an exact formulation of scattering from large aspect ratio targets in a waveguide, and he has written a number of fundamental articles on scattering from shells and large aspect ratio targets. He is also the sole developer of the computer simulations PC SWAT and Imaging SWAT.

Jose E. Fernandez has been working at the Coastal Systems Station since 1984, where he has been involved in the design, testing and data analysis of several sonar systems. He is currently working in the area of synthetic aperture sonar. His research interests include self-cohering of arrays, adaptive array systems, synthetic aperture and modern beamforming and spectral estimation techniques and their application to sonar systems.

Leonid Vaizer became an electronics engineer at the Coastal Systems Station in 1984. There he had worked in the areas of parameter estimation, design and analysis of the navigation algorithms, target motion analysis, target localization algorithms from the magnetic data. Recently Mr. Vaizer has been working on the motion compensation and beamforming algorithms for the Synthetic Aperture Sonar.

John D. Lathrop is currently senior scientist at Coastal Systems Station, where his expertise in the fields of acoustics, optics, and magnetics are frequently required. He headed the original MADOM project, which successfully demonstrated a low frequency synthetic aperture sonar. He is currently helping coordinate the Joint Counter Mine ACTD.

Mr. Robert W. Sheriff has twenty years of experience in acoustic sensor technology development. His activities over the past six years have been focused towards high resolution synthetic aperture side-look sonars. In particular, he has had a key role in the design of the synthetic aperture used in the U.S. Navy's shallow water sensor suite (High

Frequency/Low Frequency Synthetic Aperture Sonar). He is presently the lead analyst for the synthetic aperture sonars under development at Northrup/Grumman.

Mr. James T. Christoff has been involved in the development of high resolution synthetic aperture sonar (SAS) for mine hunting applications for the past twenty years. He is currently working in the area of self-cohering SAS, adaptive beamforming of conventional and synthetic arrays, and the adaptation of modern signal processing techniques to high resolution imaging sonar systems. Most recently he has served as the project engineer for the High Frequency/Low Frequency Synthetic Aperture Sonar.

Mr. Thomas C. Montgomery has been employed at Northrop Grumman Oceanic Systems since 1981. He is currently an engineer in the SONAR systems group. Mr. Montgomery has been working in the area of high resolution Synthetic Aperture SONAR for proud and buried detection for 5 years.

REFERENCES

1. R.S. Raven, "Electronics stabilization for displaced phase center systems", United States Patent 4,244,0336, Jan 1981.
2. R.W. Sheriff, "Synthetic aperture beamforming with automatic phase compensation for high frequency sonars", Proceedings of the 1992 Symposium On Autonomous Underwater Vehicle Technology, pp. 236-245, July 1992.
3. L. Vaizer, J.T. Christoff, J.D. Lathrop, and G.S. Sammelmann "Motion Compensation for High Frequency Sonars", presented at Nov. 1994 ADPA conference.

Automated Detection/Classification of Sea Mines in Sonar Imagery

Gerald J. Dobeck, John C. Hyland and Le'Derick Smedley

Naval Surface Warfare Center, Dahlgren Division, Coastal Systems Station, Panama City, Florida

Abstract

An advanced capability for automated detection and classification of sea mines in sonar imagery has been developed. The Advanced Mine Detection and Classification (AMDAC) algorithm consists of an improved detection density algorithm, a classification feature extractor that uses a stepwise feature selection strategy, a k-nearest neighbor attractor-based neural network (KNN) classifier, and an optimal discriminatory filter classifier (ODFC). The detection stage uses a nonlinear matched filter to identify mine-size regions in the sonar image that closely match a mine's signature. For each detected mine-like region, the feature extractor calculates a large set of candidate classification features. A stepwise feature selection process then determines the subset features that optimizes probability of detection and probability of classification (PdPc) for each of the classifiers while minimizing false alarms.

The AMDAC has been tested using 335 sonar images from three different sonar systems: a synthetic aperture sonar (SAS with 255 images), a side-scan sonar (SSS1 with 60 images) and another side-scan sonar (SSS2 with 60 images). The AMDAC's performance is: 90% PdPc with 0.42 false alarms per image for the SSS1; 92% PdPc with 0.64 false alarms per image for the SAS; and 91% PdPc with 0.12 false alarms per image for the SSS2. For these data bases the algorithm's performance is as good or slightly better than that of an expert sonar operator.

This work was funded by the Office of Naval Research, ONR 321TS, through the 6.2 Mine Countermeasures program element.

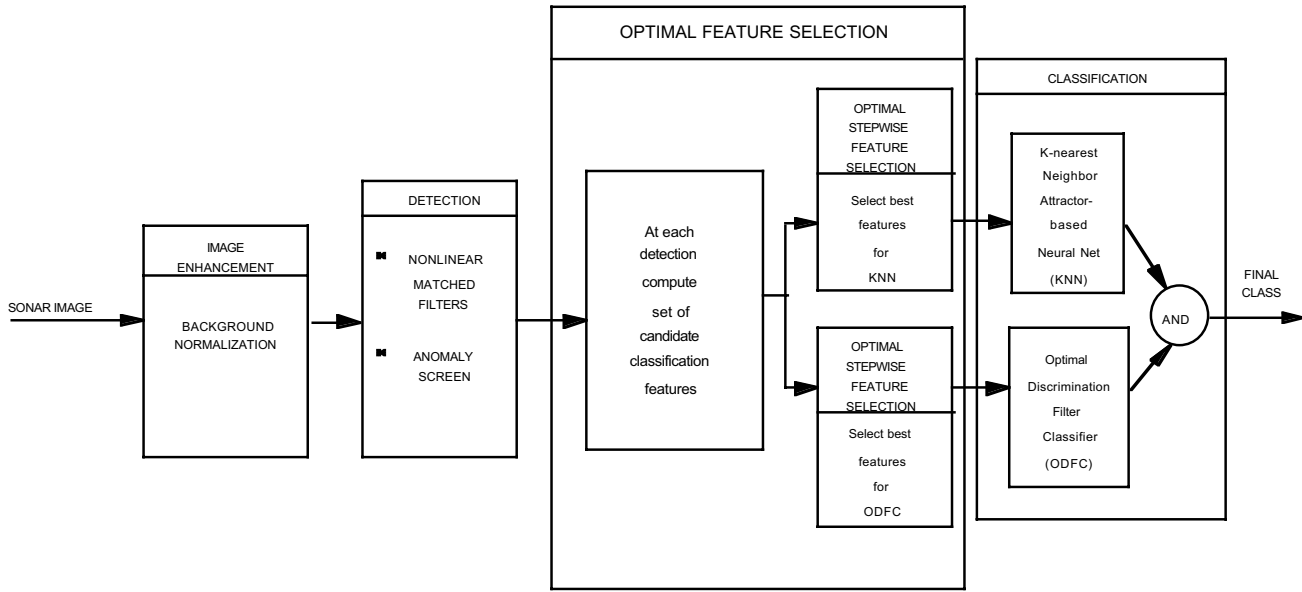
1. Introduction

This paper builds on our earlier work [1] and describes a new algorithm for the automated detection and classification (D/C) of sea mines in sonar imagery. Three sonar image data bases are used to evaluate the new D/C algorithm. The algorithm is referred to as the Advanced Mine Detection and Classification (AMDAC) algorithm. It is comprised of four stages: (1) Image Enhancement, (2) Detection, (3) Feature Extraction and Optimal Feature Selection, and (4) Classification (see Figure 1).

For the last seven years CSS has used three side-looking sonar data bases to evaluate mine detection and classification (D/C) algorithms developed in house, by industry and by academia [2], [3], [4], [5]. The data bases consist of a 255 image set from a synthetic aperture sonar (SAS), a 60 image set from a side-scan sonar (SSS1), and a 60 image set from another side-scan sonar (SSS2).

These data bases were selected because they demonstrate a variety of problematic issues and signal processing challenges. Mine threats in these data bases are bottom mines; they provide a significantly greater challenge to detect and classify than volume mines. Results for probability of detection and classification (PdPc) and false alarm rates referred to in this report are for single pass (one look) sonar operation. Single pass operation is of interest because of the implied higher search rate. Performance of an expert sonar operator was available for two of these databases, thus providing a benchmark for automated algorithm performance. Because these three data bases are somewhat small and do not represent all interesting scenarios, one must be cautious

Figure 1
Overview of AMDAC Algorithm.



in generalizing any conclusions. However, the prohibitive cost of collecting and processing large data bases makes utilization of small data bases the typical practice when evaluating and comparing automated D/C algorithms. Real sonar image data is preferred over simulated sonar data because sonar simulations are expensive and do not capture all the critical dynamics associated with actual sonar images.

The following sections, 2.1 through 2.6, describe the four stages of the AMDAC.

2. AMDAC Algorithm

2.1 Image Enhancement

The purpose of the image enhancement stage is to precondition the image so that the subsequent detection and classification stages are robust to variations in background level. This is accomplished by normalizing the background throughout the image to a constant level so that highlight and shadow levels are consistent and clearly stand out.

The principal reasons for variations of bottom brightness are (1) inadequate range-varying gains that are applied to the sonar return to compensate for the range-dependent reduction in signal strength cause by spherical spreading of acoustic energy, (2) the strong sonar returns from highly reflective bottom regions (e.g., gravel), and (3) the weak sonar returns from highly absorbent regions (e.g., mud). Thus, pre-

conditioning reduces some of the background invariance and reinstates some degree of robustness to bottom variation.

For the three sonar data bases studied in this article the inadequate range-varying gain problem, as described above, was the dominate factor; so a simple range normalization was found to be adequate. This was done as follows.

$$I_r(i,j) = \text{raw 8-bit sonar image } (0 \leq I_r(i,j) \leq 255)$$

$$i = \text{range index} \quad (1 \leq i \leq n)$$

$$j = \text{cross-range index} \quad (1 \leq j \leq m)$$

$$I_n(i,j) = \text{normalized image } (0 \leq I_n(i,j) \leq 4)$$

$$= \text{MIN} (4, I_r(i,j)/b(i))$$

where

$$b(i) = \text{mean level of } I_r \text{ at range } i$$

$$= \frac{1}{m} \sum_{j=1}^m I_n(i,j)$$

Note the following facts about I_n :

- (1) The mean background pixel intensity is essentially unity.
- (2) The dynamic range for highlight pixel intensity is from 1 to 4.

(3) The dynamic range for shadow pixel intensity is from 1 to 0.

Experience of expert side-looking sonar operators has shown that the above scaling procedure is a good way to distribute the dynamic range between highlight and shadow.

In subsequent discussions we will make use of these three facts in setting parameter values. As an aside, it has been found that images from other environments may contain many large irregular regions, some of which are highly reflective while others are highly absorbent. In these cases the simple range normalization does not achieve the goal of making the background level uniformly near unity. Other computationally more intensive methods are needed that normalize the image based on local statistics within the image. As an example, low-pass median filtering has performed quite well for us.

2.2 Detection Stage

The purpose of the detection stage is to scan the entire image and identify candidate mine-like regions that will be more thoroughly analyzed by the subsequent classification stages. This is the most computationally intensive stage because a mine-size region surrounding each image pixel must be evaluated. Therefore, the goal is to keep the computations involved with each mine-size region small. The purpose of this computation is primarily not to determine mine-likeness but rather to screen out the non mine-like regions in the vast majority of the image and thus reduce the amount of data that must be processed by the computationally more intense classification stages. If the detection stage can reduce a typical image to about 10 detections (10 being very generous), the computational requirements of the classification stages are insignificant when compared to the detection screening.

The detection stage of the AMDAC is an improvement on the one reported in our earlier paper [1]. The detection stage operates on the normalized image. The algorithm divides the image into regions along range to account for the variability of the background and mine signature as a function of range. For this study the image was divided into three regions. Next, the image is convolved with a nonlinear matched filter, a different matched filter for each of the range regions. The procedure sets negative values from the match filter to zero. For each range region the resulting matched-filtered image is normalized by removing the region's mean and dividing by the region's standard deviation. Next, the procedure scans a target-size window over the normalized matched-filter image. A detection is declared by counting the total number of pixels within the window that exceed a specified "amplitude-detection threshold"; a pixel count above the specified "detection-count threshold" is declared a target.

2.3 Nonlinear Matched Filter

The nonlinear matched filter is the work horse of the detection stage [6]. The matched-filter mask contains four distinct regions: pre-target, highlight, dead zone and shadow/post-target; see Figure 2. It is defined as,

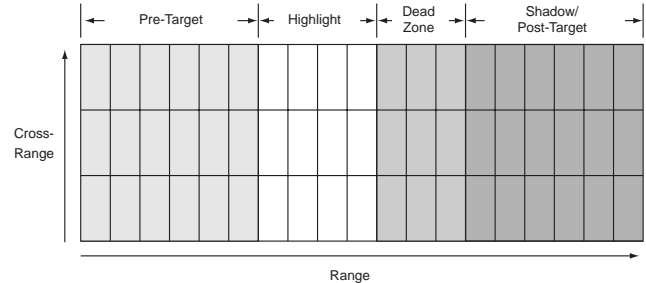
$$I_m(i, j) = \sum_{k=-N_1}^{N_2} \sum_{l=-M_1}^{M_2} g(h(k, l), I_n(i + k, j + l))$$

where

$$g(h(k, l), I) = \begin{cases} h(k, l) (I-1) & \text{for } h(k, l) \text{ corresponding to} \\ & \text{shadow, highlight, and dead zone regions} \\ h(k, l) |I-1| & \text{for } h(k, l) \text{ corresponding to pre-} \\ & \text{target region and post-target regions} \end{cases}$$

Note that the nominal background level of unity is subtracted from I .

Figure 2
Target Signature Mask.



In each of the four regions, the matched filter coefficients are constant and defined by,

$$\begin{aligned} \text{shadow region or post-target region: } h(k, l) &= 1/(S_a(S_0 - 1)) \\ \text{highlight region:} &= 1/(H_a(H_0 - 1)) \\ \text{dead zone region:} &= 0 \\ \text{pre-target and post-target regions:} &= -1/(T_a(T_0 - 1)) \end{aligned}$$

where

S_a = area of shadow region in square pixels (see Tables 1, 2 and 3)

S_0 = reference shadow level = 0.75 for this study

H_a = area of highlight region in square pixels (see Tables 1, 2 and 3)

H_0 = reference highlight level = 1.5 for this study

T_a = area of pre-target region in square pixels (see Tables 1, 2 and 3)

T_0 = reference anomalous background level

The following two anomalous levels used in this study result in the same $h(k,l)$ value.

$$T_0 = \begin{cases} 2.0, \text{ anomalous high background level} \\ 0.0, \text{ an anomalous low background level} \end{cases}$$

In this study the reference center $h(0,0)$ corresponds to the center pixel of the highlight region. The following is a brief discussion of this matched filter.

The nonlinearity is associated only with the pre-target and post-target regions. The intent of this part of the matched filter was to prevent the detection of objects with highlights or shadows that were greater than mine size. The filter coefficient for this region is negative; thus, the output of the filter is decreased if the pre-target or post-target regions are dominated by low or high valued pixels. This region could have been selected to encircle the typical mine-size area. However, the large variations in the mine's cross-range size and shadow length, together with considerations of the extra computational burden, led us to use only the area in front of the highlight region. Since the mines in our SAS image data base have no shadows, a post-target region was used in place of the shadow region.

The selection of the coefficients, defined by the refer-

ence levels and the region's area, was done to make the contribution from each region of the matched filter equal for typical shadow, highlight, and anomalous background levels. Specifically, the coefficients are constructed such that the contribution for each region is unity when evaluated at the reference level of that region.

The optimal detection-amplitude and detection-count threshold pair is selected from the optimal receiver operator characteristics (ROC) table [6]. The ROC table contains optimal threshold pair that gives the least false alarm rate for a given P_d . A computationally fast method was developed to generate the ROC table that requires only a single pass through the data base.

The AMDAC uses a different filter mask for each mine type and each range region. For example, the SAS sonar has one mask for detecting mine type "A" in the first region, another mask for detecting mine type "A" in the second region, and another mask for detecting mine type "A" in the third region. To detect a different mine type, three different masks would be used. Reference [1] discusses target mask design in detail. Tables 1 through 3 show the masks' sizes for the three sonars and the three range regions.

2.4 Feature Extraction

In the feature extraction stage, a large set of classification features is computed from a target-size classification window centered at each detection location in both the normalized raw sonar image and the normalized matched-filtered image. The procedure calculates forty-five candidate features based on the size, shape and strength of the highlight and shadow, and histogram information of pixel intensity within the classification window. A complete list of features follows:

1. W_{pix} : number of normalized image pixels in the window that exceed a threshold*
2. Mfw_{pix} : number of matched-filter pixels in the window that exceed a threshold
3. M_{wpix} : maximum normalized image pixel intensity in the window
4. Mmf_{wpix} : maximum matched-filter pixel intensity in the window
5. T_{str} : target strength computed from the normalized image image
6. Mft_{str} : target strength computed from the matched-filter image
7. Mx_{eig} : length of major axis of an ellipse fit to highlight region of the normalized image
8. Mn_{eig} : width of minor axis of an ellipse fit to highlight region of the normalized image
9. $Mfmx_{eig}$: length of major axis of an ellipse fit to bright region of the matched-filter image

Table 1. Target Mask Size for SSS1				
Image Region	Mask Region			
	Pre-Target	Highlight	Dead Zone	Post-Target
First Region	12x3	5x3	4x3	10x3
Second Region	12x3	5x3	4x3	14x3
Third Region	12x3	5x3	4x3	20x3

Table 2. Target Mask Size for SAS				
Image Region	Mask Region			
	Pre-Target	Highlight	Dead Zone	Post-Target
First Region	12x3	9x3	0x3	12x3
Second Region	12x3	9x3	0x3	12x3
Third Region	12x3	9x3	0x3	12x3

Table 3. Target Mask Size for SSS2				
Range Region	Mask Region			
	Pre-Target	Highlight	Dead Zone	Shadow
First Region	10x3	3x3	3x3	5x3
Second Region	10x3	3x3	3x3	11x3
Third Region	10x3	3x3	3x3	11x3

10. Mfmn_eig: width of minor axis of an ellipse fit to bright region of the matched-filter image
 11. S_len: shadow length
 12. S_str: shadow strength
 13. Mmf_pclu: maximum matched-filter intensity over the pixels in the detection cluster
 14. C_pix: number of pixels in the detection cluster
 15. C_im: number of detected clusters in the image
 - 16 - 25. Hist_org(i): number of normalized pixels above threshold(i) in the window, i from 1 to 10
 - 26 - 35. Hist_mf(i): number of matched-filter pixels above threshold(i) in the window
 - 36 - 45. Hist_diff(i): number of matched-filter pixels above threshold(i) in the classification window minus the number of matched-filter pixels above threshold(i) in the region that locally surrounds the classification window
- * All thresholds are selected by the designer.

2.5 Optimal Feature Selection

When training classifiers with finite databases, Bellman discovered that the robustness of a classifier will collapse when the number of features becomes too large [7]. This is known as “the curse of dimensionality.” Therefore, an important part of the overall classifier design is to select a small and robust set of classification features from the larger candidate set. Evaluating all possible combinations of 45 features is computationally not feasible (there are $2^{45} - 1$ combinations, a number greater than 10^{12}). Therefore, a stepwise optimal selection process is used (select the best single feature, next select best of the remaining 44 features to add to the first, next select to best of the remaining 43 features to add to the previous two, etc.) [8]. For a 45 feature set this involves evaluating 1035 feature combinations. Computationally efficient algorithms have been developed for this selection process.

The two classifiers used in this algorithm were the k-nearest neighbor neural network (KNN) and the optimal discriminatory filter classifier (ODFC). Since two classifiers are used in this detection/classification algorithm, there are two selection algorithms; each one is tuned to the respective classifier. This is required because a set of features that is optimal for one classifier will, in general, be far from optimal for the other classifier. This usually results when each classifier uses a different mathematical/geometrical structure to partition feature space into class regions. A set of features amenable to one partitioning scheme may not separate well for a different partitioning scheme.

Briefly, two feature selection algorithms were developed for the KNN and ODFC, respectively. By optimal is met the following. Bellman’s curse of dimensionality implies that, for a finite training set, the detection and classification performance (as judged by the validation/test set) does

not continually improve as more features are added (as dimensionality is increased) to the classification process. With a finite data set it is possible only to determine a subset of features that will give robust performance. Optimal selection in this context means finding the subset of features from a much larger set that gives the best performance for both the finite training and validation (test) sets for a specific classifier (in our case, either KNN or ODFC). Specifically, the best subset is the subset of features which when fed into the classifier minimizes a risk metric. The risk metric that is used is defined as the maximum (between the training and validation data sets) of the weighted sum of the number of missed mines and number of false calls. As stated above, for a typical candidate feature set of size 45, there would be $2^{45} - 1$ combinations of subsets to evaluate in order to determine a global optimum. Because this is too large of a number to evaluate, a Forward Stepwise Optimal Selection Process (FSOSP) is used instead of a Globally Optimum Selection process. The FSOSP selects as the first feature the one that gives the best classifier performance of any single feature. The second feature selected is the one that performs best when used with the first. As its name implies, the Forward Optimal Stepwise Selection Process continues at each stage by adding a new feature to the subset determined in the previous stage. This stepwise process is obviously not globally optimal, but has worked extremely well in this optimization application. Our research suggests that it is important that the classifier itself be used in the selection process. Other selection techniques (e.g., principal component analysis or multivariate normal models) are often used because they are computationally tractable. But they are usually not based on the same mathematical, statistical, or geometrical structure as the classifier and, therefore, do not select the best features for that classifier. Keeping in mind Bellman’s curse of dimensionality, our research suggests that classifiers that train fast, for which the best subset of features can be optimally selected, will perform significantly better than more sophisticated classifiers for which the best subsets cannot be found because training is too computationally expensive.

The selection process has been further improved by adding a Backward Stepwise Optimal Selection Process (BSOSP) analogous to model order reduction used in statistics [9]. Because the candidate features are not orthogonal, adding a new feature to the current optimal feature subset can in fact decrease the performance metric; this is consistent with Bellman’s curse of dimensionality. The augmented procedure is to first use the FSOSP to determine the initial feature set as previously described. Then, the BSOSP determines which features to remove. Application of the FSOSP and BSOSP can be repeated until performance improvement stops. As an example, using the SSS2 data base, the number of false alarms per image decreased from 0.28 (using only FSOSP) to 0.12 (using FSOSP followed by BSOSP) for the same PdPc of 91%.

2.6 Classification

The KNN and ODFC classifiers were chosen because they process the data using significantly different mathematical, statistical, and geometrical paradigms; “ANDING” the two classifiers produces highly effective results. In general, many classifiers could be “ANDED” but for the sonar data presented here, two have worked very well. Also the process of classifier selection relied strongly on the fact that the optimal feature selection process employed would be “tuned” to each classifier. With this in mind the two classifiers were chosen because: (a) they train very fast - this fact makes the algorithm used in the stepwise optimal selection process feasible, (b) they each divide feature space into different geometrical models — the KNN into hyperspheres and the ODFC into hyperplanes — this tends to make the classifiers complementary, (c) the classifiers use different “noise” tolerant paradigms. The KNN uses sample Bayesian conditional probabilities as determined from the training data. The ODFC uses noise rejection and signal enhancement schemes based on concepts of matched-filter design.

The KNN is a probabilistic-based neural network that employs radial-basis neurons [10]. The neural network has two layers: the attractor layer and the confidence layer. The attractor layer is constructed during training in the following way. Feature space is partitioned by a set of attractors. A feature vector, f , is said to belong to attractor i if $N(f, f_i) < R_i$ where $N(f, f_i)$ is some distance measure between vectors f and f_i (for this study an L_2 norm was used), f_i is the center of attractor i and R_i is the radius of attractor i .

For a given $N(\dots)$, R_i , and f_i the probability that attractor i contains a given class can be estimated from sample probabilities computed from the training set. Each attractor is represented as a radial-basis neuron that has the feature vector as an input and multiple outputs (one output for each class). The i -th neuron *fires* when the input feature vector belongs to attractor i ; when it fires, the level of each output, associated with a given class, equals the estimated probability that the attractor contains that class.

During training, the number of attractors, their center locations (f_i), radii (R_i), and degree of overlap are determined in an optimal fashion to encompass the entire training set. The radii are selected using the well-known k-nearest neighbor scheme to achieve accurate probability estimates and adequate class boundary resolution for good class discrimination. The more training samples in an attractor, the more accurate the sample probability estimates will be. In a relative sense, an attractor with a large radius will encompass a large number of training samples. However, the size of the radii is balanced against the resolution into which feature space is partitioned; the smaller the radii, the better the discriminatory resolution at complex class boundaries. Finally, attractor overlap is used to regulate the *smoothness* of probability estimates across class boundaries.

Training of this neural network also takes into account that the training data is usually statistically unfairly sampled; i.e., the number of training samples in a class (or subclass) does not reflect the true probability of occurrence of that class but instead reflects the artificial conditions over which the data was collected. For example, one might have more of one class than another, or more data collected under one condition than another. In reality, fairly sampled data is seldom available because the cost to collect an adequate data base is unacceptably high or simply because one does not have adequate access to another country's targets or environment in which to collect representative data. Under such uncertainty, it was determined that the best statistical property to reinstate into the training set is that of equally likely classes (or subclasses). This is accomplished by a specially devised counting method that is used to determine the sample probabilities. Thus, the training of this neural network is not biased to favor those classes that were most plentiful in the training and test sets and to ignore those classes that were least abundant. Other neural network training algorithms that optimize the number of correct classifications are typically biased by such data.

The output of the attractor layer is then fed to the confidence layer which determines the confidence that the input feature vector belongs to each class. First all the attractors that contain the input feature vector (or are sufficiently near it) are identified. The confidence that the feature vector belongs to a given class is then determined by interpolating the individual probability estimates that the feature vector belongs to a class over this set of attractors. In the interpolation, the contribution of each attractor's probability estimate is weighed according to how close the feature vector is to the attractor's center.

This neural network has the desirable characteristic that it can determine if a feature vector cannot be reliably classified. Specifically, if there are no attractors sufficiently near, then the feature vector is considered statistically different than the training vectors and is said to belong to an unknown class. Another way to view this is to say that during training, the neural network never experienced anything that was representative of this new vector (i.e., the new vector is not within the neural network's experience base). Under this circumstance, there is no basis to select among the known classes and all outputs of the neural network are set to zero. Other noteworthy characteristics of this network are that the training algorithm is non-iterative, fast and the network sizes are reasonable thereby permitting very quick execution so specialized hardware is not needed.

The ODFC is a classifier with its basis in linear discrimination theory [10]. Two banks of linear filters are determined from the training set: one bank is sensitive to mine characteristics and the other is sensitive to clutter characteristics. The following is a brief description on how the discrimination process works.

Let f be a feature vector. Let $F_m(f, i)$ be the energy

output for input f of the i -th filter in the mine-filter bank, and $F_c(f,j)$ be the energy output for input f of the j -th filter in the clutter-filter bank. F_m and F_c are linear filters; the outputs of these filters are linear combinations of the input features plus a DC offset and a warping term made up of a linear combination of nonlinear functions of the features. The filter's coefficients, DC offset, and warping coefficients are determined such that, on the average, the energy output of the mine-filter bank is greater than the energy output of the clutter-filter bank when the input feature vector corresponds to a mine. And vice versa for a feature vector that corresponds to clutter. That is, on the average,

$$\max_i F_m(f(\text{mine}),i) > \max_j F_c(f(\text{mine}),j)$$

$$\max_i F_m(f(\text{clutter}),i) < \max_j F_c(f(\text{clutter}),j)$$

The solution involves the solving of a generalized eigenvalue problem. In the ODFC linear combinations of features permit boundaries between classes to be described by sets of hyperplanes. By adding a linear combination of nonlinear functions of the features one changes the hyperplane surface to one that is curved (warped). These nonlinear terms permit the partitioning surfaces in feature space to more efficiently fit irregular class boundaries.

Classification is determined by “ANDING” the output of both classifiers. Both the KNN and ODFC have two outputs corresponding to the confidence that the input feature vector is associated with a mine or clutter. Let $C_{knn}(\text{mine})$ and $C_{knn}(\text{clutter})$ designate these two confident levels for the KNN; and $C_{odfc}(\text{mine})$ and $C_{odfc}(\text{clutter})$ for the ODFC. If

$$T_{knn} C_{knn}(\text{mine}) > C_{knn}(\text{clutter})$$

AND

$$T_{odfc} C_{odfc}(\text{mine}) > C_{odfc}(\text{clutter})$$

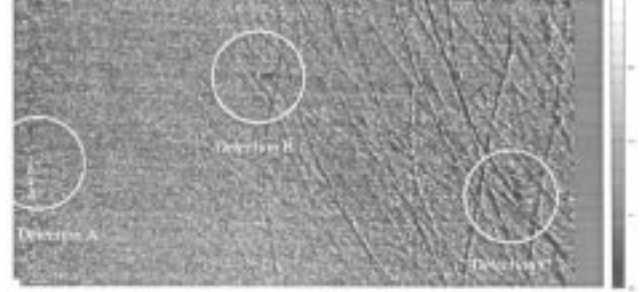
a mine classification is declared. The classification gain thresholds, T_{knn} and T_{odfc} , are adjusted to select the desired balance between PdPc and false alarms.

3. Results

3.1 SSS2 Example 1

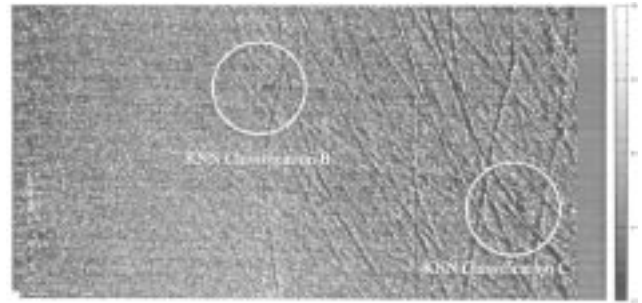
In Figures 3 through 10, Image 0 and Image 51 from the 60 image SSS2 data base are used to illustrate the D/C algorithm. Figure 3 shows the normalized image and the results of the detection stage. The gray scale indicator on the extreme right of the image indicates pixel intensity. White indicates a pixel intensity of 4.0 and represents the maximum pixel intensity value displayed. Black indicates a pixel

Figure 3
Detections for SSS2 Image 0.



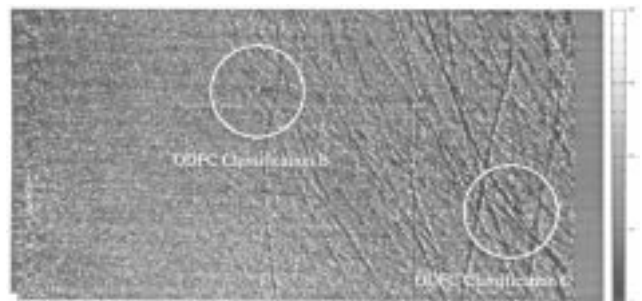
intensity of 0.0 and represents the minimum pixel intensity value displayed. To give a size perspective, each sonar image has a two-meter by two-meter square highlight in the lower left-hand corner of the image. In all images, range from the sonar increases from left to right implying target

Figure 4
KNN Classifications for SSS2 Image 0.



shadows are to the right of the highlights. The detected mine-like targets typically resemble the target-signature mask—a highlight region followed by a shadow and preceded by a uniform background. With a strong highlight and pronounced shadow, Detection B is easily visible. Although Detection C

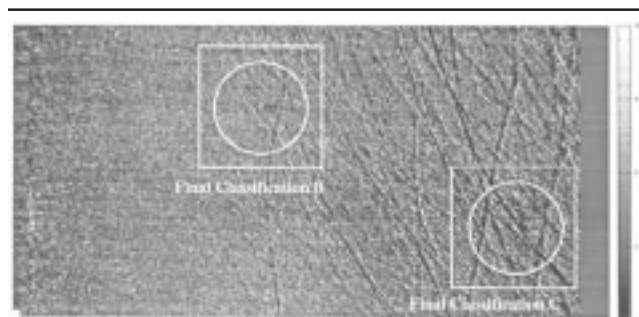
Figure 5
ODFC Classifications for SSS2 Image 0.



has a noticeable highlight followed by a shadow, the shadow's proximity to a trough made by a fisherman's drag net obscures the shadow region. False Detection A is triggered by a subtle highlight and shadow.

Figures 4 and 5 show that both the KNN and the ODFC classify Detections B and C as mine-like; they both reject Detection A. "ANDING" the two classifiers results in Final Classifications B and C as illustrated in Figure 6. The squares in Figure 6 indicate actual mines; there one sees that both mines are detected and classified and one false target is detected but not classified as mine-like by either classifier.

Figure 6
KNN and ODFC Classifications for SSS2 Image 0.



3.2 SSS2 Example 2

Figure 7 shows another SSS2 example. This particular image illustrates some of the difficulties associated with normalizing the background in the sonar image. Note that the background level of the image is not uniform. And there is a large band of bright pixels that extends from the upper left to the lower right of the image caused by a highly reflective bottom type. Despite the lack of uniformity in the background intensity, the AMDAC detects four candidate mines.

In Figure 8, the KNN classifies only Detections D and E as mines and rejects Detections C and F. Figure 9 shows

Figure 7
Detections for SSS2 Image 51.

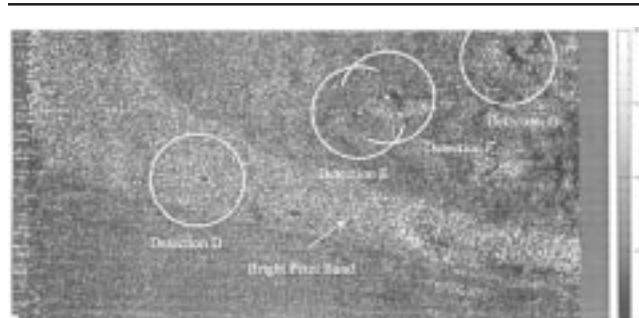
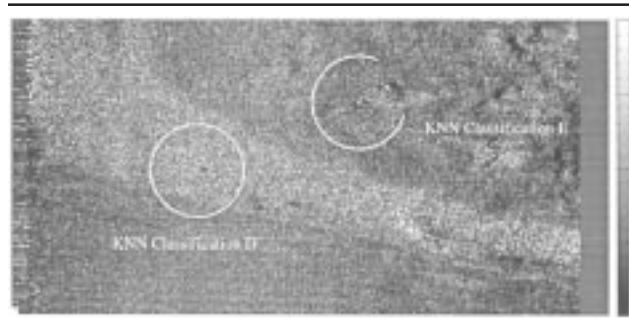
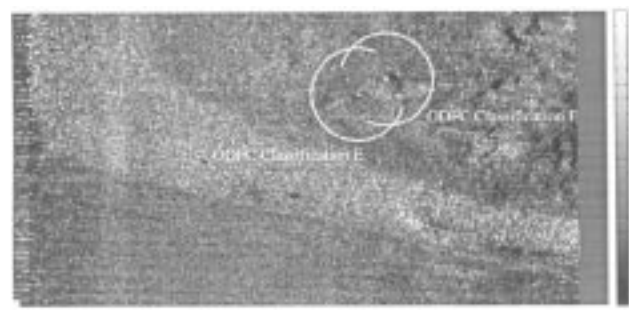


Figure 8
KNN Classifications for SSS2 Image 51.



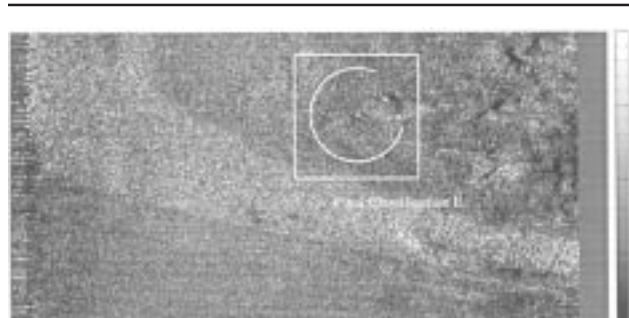
that the ODFC classifies Detections E and F as mines and rejects Detections C and D. Results from "ANDING" the two classifiers are shown in Figure 10. As the ground truth square indicates, the final mine classification is correct and

Figure 9
ODFC Classifications for SSS2 Image 51.



all false alarms have been eliminated. This example clearly illustrates the power of combining two different classification approaches; separately, each approach would have had one correct classification and one false alarm. "ANDING" the two classifiers eliminated the false alarms.

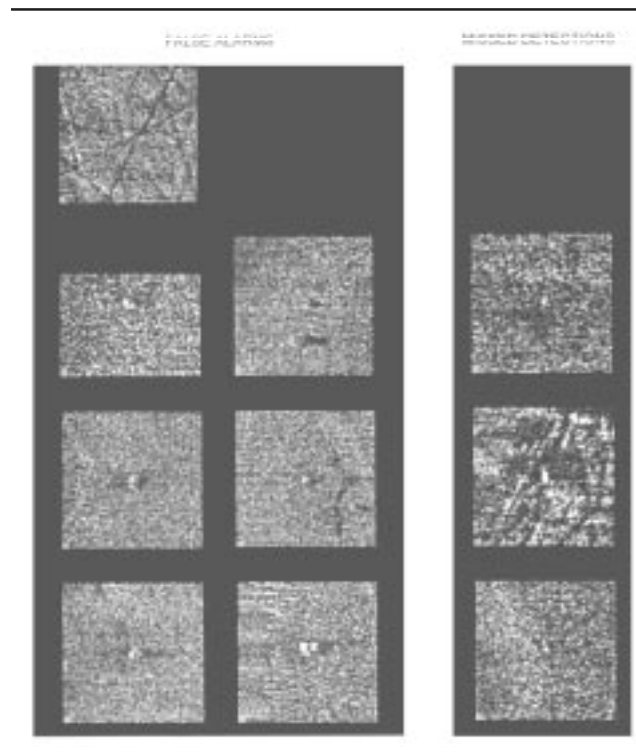
Figure 10
KNN and ODFC Classifications for SSS2 Image 51.



3.3 SSS2 False Alarms, Missed Detections and Overall Performance

Overall, the AMDAC detected and classified 91% of the mines in the SSS2 data base with an average false alarm rate of 0.12 false alarms per image. Figure 11 shows the seven false alarms detected and three missed mines in the entire SSS2 data base. The false targets are quite mine-like. The top and bottom missed mines in Figure 11 have weak highlights and very poor shadows. The middle missed mine is embedded in very bright surface reverberation which made the mine signature blend in with the background.

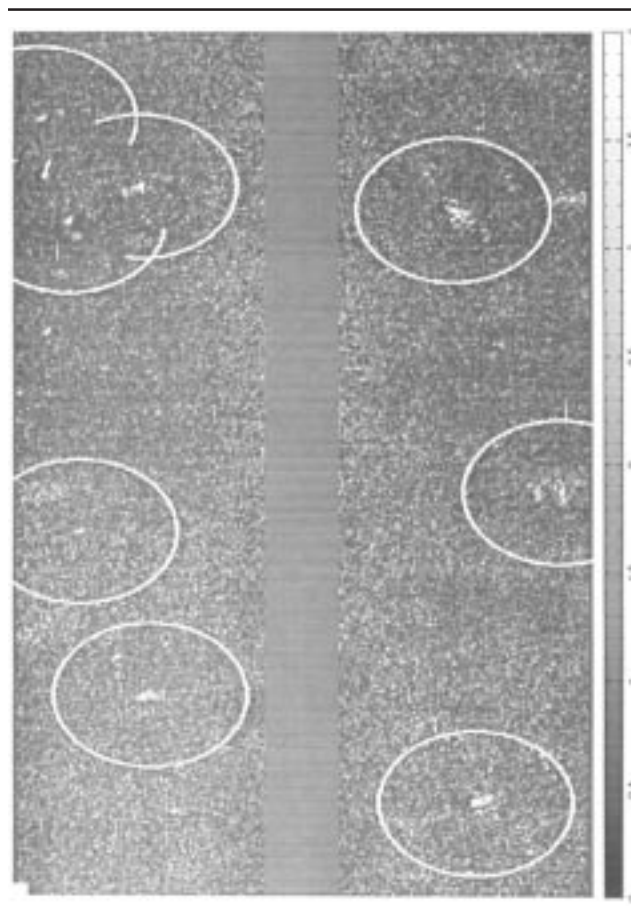
Figure 11
False Alarms and Missed Detections for SSS2.



3.4 SAS Example

In Figures 12 through 15, Image 116 of the 215 image SAS image data base is used to further illustrate the D/C algorithm. The sonar image contains data from both the starboard and port sides of the sonar. Returns from the water column in the middle of the sonar image were blanked out prior to processing. Sonar operators ignore this region because it consists of returns from the water volume prior to the first bottom return. Note that there are no shadows on

Figure 12
Detections for SAS Image 116.



the targets; because the data was collected during shallow water operations, surface reverberation came into play and filled in the shadows. The lack of a target shadow makes the detection and classification process quite difficult. When a target exhibits only a highlight, the detection thresholds are typically set to accept a higher false detection rate. The classification phase is then relied upon to reject the extra false targets that are detected.

Figure 12 shows that the AMDAC has detected eight mine-like regions in the SAS image. All eight candidate regions do exhibit the desired mine-size highlight surrounded by a uniform background. Figure 13 shows that the KNN rejects two of the detections and Figure 14 shows the ODFC rejects five of the detections. “ANDING” the classifiers results in the classification of the two mines and one false target as shown in Figure 15.

3.5 Results Summary

Table 4 summarizes the AMDAC’s performance for the all three sonars, the SSS1, the SAS and the SSS2. Table

Figure 13
KNN Classifications for SAS Image 116.

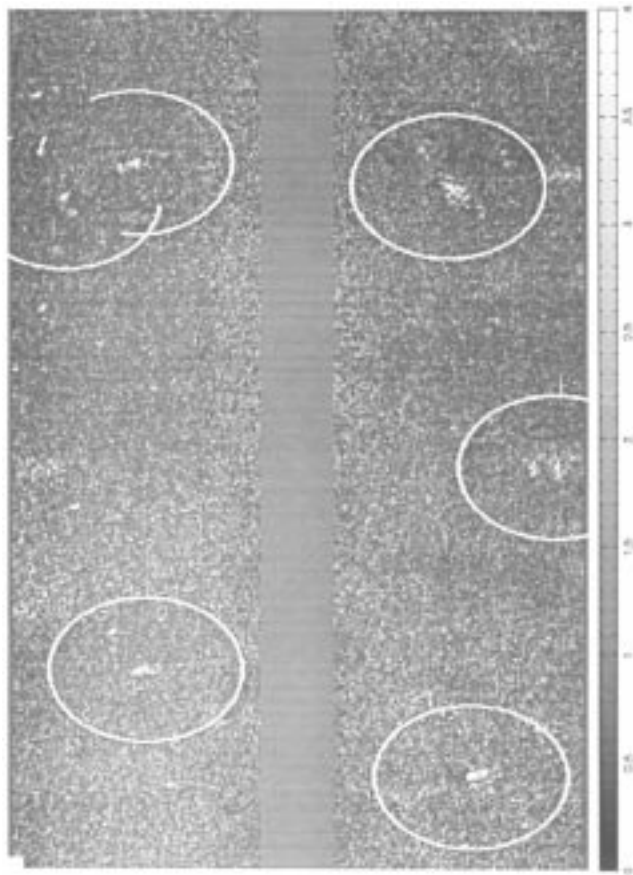
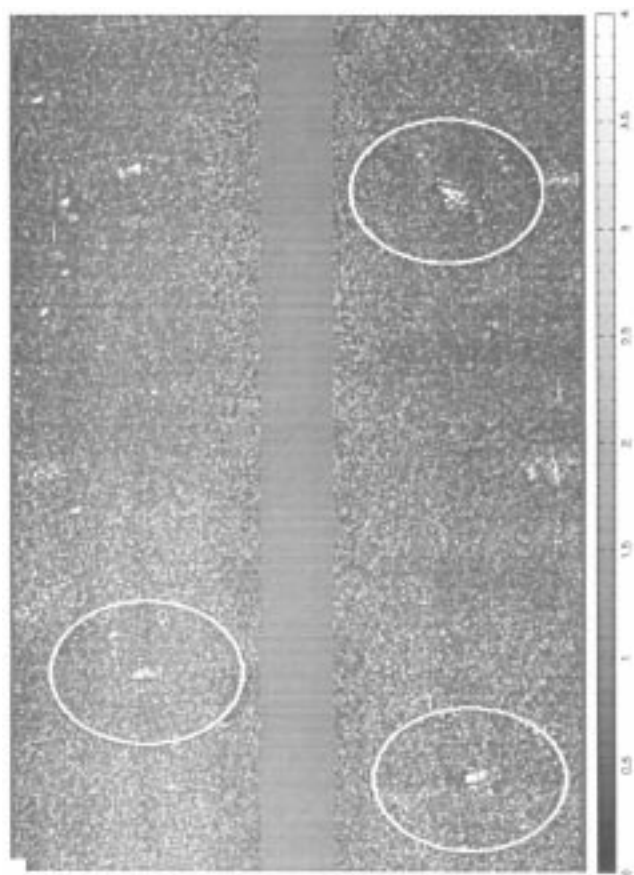


Figure 14
ODFC Classifications for SAS Image 116.



4 also lists expert sonar operator's performance for the SSS1 and SAS data bases. Operator performance for the SSS2 is unavailable. Because of the similarities between the SSS1 and the SSS2, the operator performance for the SSS2 should be comparable to that of the SSS1.

For the SSS1, the AMDAC detects and classifies 90% of the mines with 0.42 false alarms per image while the expert operator detected 80% with 0.72 false alarms per image. For the SAS, the AMDAC performs similarly to the expert sonar operator at 68% PdPc. However, the AMDAC can also be adjusted to 92% PdPc with 0.64 false alarms per image. And for the SSS2, the AMDAC shows an impressive 91% PdPc with only 0.12 false alarms per image.

Table 4. AMDAC Performance Summary				
Sonar	Operator		AMDAC	
	PdPc (%)	Fa/Image	PdPc (%)	Fa/Image
SSS1	80	0.72	90	0.42
SAS	68	0.23	68 92	0.21 0.64
SSS2	N/A	N/A	91	0.12

4. Conclusions and Future Research

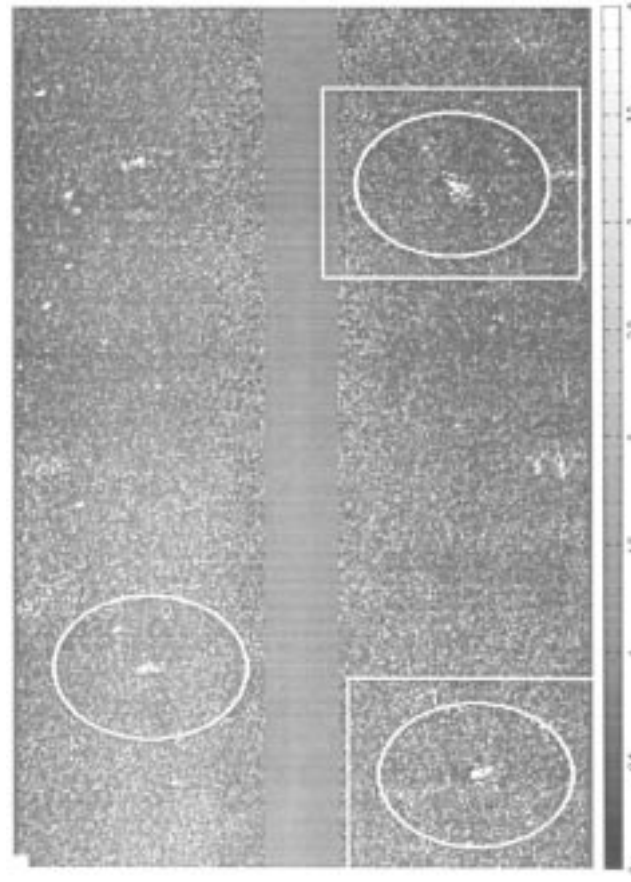
Five fundamental principles have come out of this research on automated detection and classification.

(1) The detection stage is by far the most computationally intensive stage. Because the entire image must be scanned, the basic design focus is on keeping the number of computations per pixel small. The main goal is not to detect mine-like objects, but rather to eliminate the majority of the image that is non-mine-like. The resulting detections will be processed in depth by the classification stages which require many more computations per pixel in order to extract robust and discriminatory mine-like features. If the detector produces 10 mine-like detections per image on the average (a very generous number), we have found that the computational requirements of our classification stages are negligible compared to those of the detector. It then follows that this classifier's main goal is to eliminate the false targets while preserving mine detections.

(2) The classification stage uses two classifiers: the

Figure 15

KNN and ODFC Classifications for SAS Image 116.



KNN and ODFC. The stepwise optimal selection procedure, described herein, dramatically improves the performance of each classifier by permitting a computationally efficient means to select the “best” subset of classification features from a much larger set of candidate features. As such it mitigates problems associated with Bellman’s curse of dimensionality.

(3) Significant improvement in classifier performance results if the feature selection process is highly “tuned” to the respective classifier. Classifiers use statistical, mathematical, and geometrical constructs to partition feature space into class regions. In this research we found that a subset of features optimal for one classifier’s partitioning scheme will be far from optimal for another classifier which uses a different partitioning approach. Therefore, we use the same partitioning approach when determining the best feature subset for a particular classifier.

(4) Because training procedure for both the KNN and ODFC is very fast, it was possible to develop a stepwise optimal selection procedure capable of efficiently evaluating thousands of feature combinations. Without such an automated procedure it was impossible for us to determine the

“best” features. Being able to use the “best” features dramatically improved the performance of our classifiers. This strongly suggests the following. Rapid-trainable classifiers, whose “best” features can be determined by stepwise optimal selection, may significantly outperform more complex classifiers that have computationally intense training procedures and must rely on selection methods that are either heuristic or not well “tuned” to the classifier.

(5) There is a significant improvement in overall classification performance that results from “ANDING” classifiers which use complementary statistical, mathematical, and geometrical constructs to describe class boundaries in feature space. “ANDING” the KNN and ODFC proved very adept at reducing false alarms while maintaining a high probability of mine detection and classification. This concept can be illustrated using the paradigm of “getting a second doctor’s opinion”. Two doctors look at data from a patient to arrive at their diagnoses. Even though they look at the same data, each doctor emphasizes or de-emphasizes different aspects based on their training and experience. If they conclude the same diagnosis, there is little doubt of its validity. This also suggests that “ANDING” two or more simple classifiers may lead to improved performance over a single more complex classifier. This leads the authors to believe that extremely high performance in automated mine D/C can be achieved by “ANDING” (fusing) the diverse D/C algorithms currently being developed through ONR under their Mine Countermeasures research programs.

Overall, the new detection and classification algorithm developed has been shown to perform significantly better than the detection and classification algorithm previously reported in SPIE 95 [1]. The new algorithm used in this study performs as well or slightly better than an expert sonar operator on the three sonar image data bases.

The algorithm’s robustness will be further evaluated on new advanced synthetic aperture and side-looking sonars that are currently undergoing their initial sea testing. We will investigate the benefits of using three classifiers rather than just two. Using more than three classifiers produce some combinatorial design issues. Also, algorithms that adapt detection and classification thresholds will be developed in order to increase robustness to varying environments and bottom types.

5. Acknowledgments

This work was funded by the Office of Naval Research, ONR 321TS as part of the 6.2 Mine Countermeasures program element. The technical agent for this work is the NSWC Coastal Systems Station, Dahlgren Division. The point of contact is Dr. Gerald J. Dobeck, Code 10T2, Panama City, Florida 32407-7001, Phone: 904-234-4222.

6. Biographies

Dr. Gerald J. Dobeck received the B.S. degree in physics at the University of Massachusetts in 1970 and the M.S. and Ph.D. degrees in electrical engineering at the University of South Florida in 1973 and 1976, respectively. Since 1976 he has been employed at the Coastal Systems Station, Naval Surface Warfare Center, Dahlgren Division, Panama City, Florida, where he received the 1981 and 1996 Commanding Officer/Technical Director Science and Technology Award. He is a reviewer for IEEE, ASME, and the Journal of Underwater Acoustics and has been session chair at past IEEE and SPIE conferences. His current research interests include automatic detection and classification of underwater targets in cluttered environments from synthetic and real aperture sonar imagery, the echo structure of acoustic sonar returns, underwater electro-optic imagery, and gradiometer/magnetometer signals.

Dr. John C. Hyland received the B.E. degree in electrical engineering and mathematics from Vanderbilt University in 1984 and the M.E. and Ph.D. degrees in electrical engineering from the University of Florida in 1987 and 1993. From 1987 to present he has been employed at the Coastal Systems Station, NSWC Dahlgren Division, Panama City, Florida. He has received two commendations from the Chief of Naval Research for his research into mine avoidance. He has been a reviewer of the IEEE Ocean Engineering Society Journal and has been a session co-chair at the Society for Computer Simulation Conference (SCSC). His technical experience and research interests include underwater vehicles, simulation, sonar modeling, statistical analysis of minehunting systems, and image processing.

Le'Derick Smedley received a B.S. degree in electrical engineering from Tuskegee University in 1990. Since, he has been employed at the Coastal Systems Station, Naval Surface Warfare Center, Dahlgren Division, Panama City, Florida. He has worked primarily in image processing: detection and classification, beamforming, neural network. His current research efforts are the application of neural networks to the problems of automated mine detection and classification in compressed sonar images as well as sensor fusion data.

7. REFERENCES

- [1] G. J. Dobeck and J. C. Hyland, "Sea Mine Detection and Classification Using Side-Looking Sonars," Proceedings of the SPIE Annual International Symposium on Aerospace/Defense Sensing, Simulation and Control, Vol. 2496: Detection Technologies for Mines and Mine-like Targets, 17-21 April 1995, Orlando, Florida.
- [2] M. G. Bello, "Hierarchical Multilayer Perceptron Network-Based Fusion Algorithms for Detection/Classification of Mines Using Multiple Acoustic Images and Magnetic Data," Proceedings of SPIE '96, Vol. 2765, 9-12 April, 1996, Orlando, Florida.
- [3] T. Aridgides et al., "Adaptive-Filter/Feature Orthogonalization Processing String for Optimal LLRT Mine Classification in Side-Scan Sonar Imagery," Proceedings of SPIE '96, Vol. 2765, 9-12 April, 1996, Orlando, Florida.
- [4] D. Kil and F. Shin, "The Impact of Lossy Image Compression on Automated Target Recognition Performance," Proceedings of IEEE Oceans '96, September, 1996, Fort Lauderdale, Florida.
- [5] S. Nelson and S. Tuovila, "Automated Recognition of Acoustic Image Clutter," Proceedings of SPIE '96, Vol. 2765, 9-12 April, 1996, Orlando, Florida.
- [6] H. Van Trees, Detection, Estimation and Modulation Theory, Part I, John Wiley and Sons, 1968.
- [7] R. Duda and P. Hart, Pattern Recognition and Scene Analysis, John Wiley and Sons, 1973.
- [8] K. Enslein, A. Ralston and H. Wolf, Statistical Methods for Digital Computers, Volume II, John Wiley and Sons, 1977.
- [9] L. Ott, An Introduction to Statistical Methods and Data Analysis, Third Edition, PWS-KENT Publishing Company, Boston, Massachusetts, 1988.
- [10] B. D. Ripley, Pattern Recognition and Neural Networks, Cambridge University Press, 1996.

Underwater Electro-Optical System for Mine Identification

Michael P. Strand

Coastal Systems Station, Naval Surface Warfare Center, Dahlgren Division, Panama City, Florida

1. Introduction

The Electro-Optic Identification (EOID) Sensors project is developing a Laser Visual Identification Sensor (LVIS) for identification of proud, partially buried, and moored mines in shallow water/very shallow water (SW/VSW). LVIS will be deployed in small diameter underwater vehicles, including unmanned underwater vehicles (UUVs). Since the mission is mine identification, LVIS must: (a) deliver high quality images in turbid coastal waters, while (b) being compatible with the size and power constraints imposed by the intended deployment platforms. This project is sponsored by the Office of Naval Research, as a part of the AOA Mine Reconnaissance/Hunter program.

High quality images which retain target detail and contrast are required for mine identification. LVIS will be designed to produce images of minelike contacts (MLC) of sufficient quality to allow identification while operating in turbid coastal waters from a small diameter UUV. Technology goals for the first generation LVIS are: (a) identification range up to 40 feet for proud, partially buried, and moored MLCs under coastal water conditions; (b) day/night operation from a UUV operating at speeds up to 4 knots; (c) power consumption less than 500 watts, with 275 watts being typical; and (d) packaged within a 32-inch long portion of a 21-inch diameter vehicle section.

2. Role of EO in Mine Countermeasures

Analysis of Fleet missions, including establishment of a Fleet Operating Area (FOA) and establishment of an Amphibious Objective Area (AOA) provide a framework to determine the benefit of performing identification of MLCs during reconnaissance. Identification plays a key role in reconnaissance to establish an AOA. Reconnaissance operations are conducted prior to the assault to help define the threat and to determine where mine sweeping or mine hunting must be performed. Through reconnaissance, assessments are made of the extent of the mined areas, and mine types and mine densities are determined. Mine identification is required to make these assessments. Without identification, only densities of MLCs may be obtained, and mine sweeping or mine hunting will be required over all portions of the AOA which have MLCs. With identification, mine hunting or mine sweeping may be restricted to the areas of the AOA which are mined. In typical scenarios, this can lead to a drastic reduction in mine sweeping/hunting assets required to complete the mission within the allotted time.

Identification also plays a key role in reconnaissance prior to establishment of an FOA. Prior to moving a battle group or task force into an FOA, the officer in tactical com-

mand (OTC) must be provided an assessment of the potential mine threat in the area. The tactical mine warfare officer uses data gathered by all available intelligence sources to estimate the likelihood and level of mining. The operational concept for a reconnaissance system is to use the system to verify the presence of a minefield in a specific area by locating individual mines. The system is used to sample the area of interest, with the level of sampling effort based upon a balancing of the threat estimate and tactical time constraints. If no mines are found, the OTC either decides to accept the risk and continue operations or he continues sampling to increase the confidence that no mines are present. If one or more mines are located and identified, the battle group or task force will modify their intended movement for the purpose of self-protection. This will entail continuing reconnaissance to provide the OTC with enough information to decide the best course of action; i.e., either (a) map all objects for avoidance, (b) avoid the entire minefield, (c) request and wait for clearance by mine warfare forces, or (d) reconnoiter an alternative operating area.

If reconnaissance is performed without identification, every MLC in the FOA must be avoided. The percent of operating area denied is a non-linear function of the density of MLCs and the radius of the avoidance circle around each MLC. Even quite modest densities of MLCs lead to denied areas which unacceptably restrict Fleet operating options.

In summary, mine identification is an important part of mine reconnaissance. MLCs limit the performance of mine reconnaissance systems. Without identification, MLCs must be avoided by Fleet assets (leading to denied areas) or neutralized. Denied areas can dramatically and unacceptably restrict Fleet operations options, while neutralization requires time and appropriate Fleet assets. With LVIS providing a mine identification capability to a mine reconnaissance system, only the contacts identified as mines need to be avoided or neutralized.

3. Environmental Impact on EO System Performance

Environmentally derived noise sources are principal factors limiting the performance of underwater EO imaging systems. In deep, clear ocean water, an EO imaging sensor may have a range in excess of 100 feet, while in turbid littoral waters the same sensor's range may be reduced to 5 feet or less. For underwater imaging sensors, the environmental limitations may be classified as: (a) backscatter noise, (b) blur/glow/forward scatter noise, and (c) attenuation. Backscatter noise refers to the photons which are scattered back into the receiver before reaching the target plane. Blur, glow, or forward scatter noise refers to the forward scattering of

photons which have been reflected from the target plane. Because they are scattered, they image as though they were reflected from the wrong position on the target, leading to a loss of image resolution and contrast. Finally, attenuation refers to the loss of photon signal due to photon absorption or scattering out of the field of view of the receiver. Attenuation limits signal strength at the receiver.

A major goal of EO system designers is to optimize the system design to minimize the detrimental effects of the environment. In addition to the system architecture and parameters, the performance of a given underwater EO mine countermeasures (MCM) system in a given location is determined by: (1) the Inherent Optical Properties (IOPs) of the water, and (2) the IOPs of the bottom and target.

The IOPs of the water which affect the performance of EO MCM systems currently under development include: (1) the beam attenuation coefficient $c(\lambda)[m^{-1}]$, (2) the beam absorption coefficient $a(\lambda)[m^{-1}]$, and (3) the volume scattering function $\beta(\lambda, \Theta)[m^{-1}sr^{-1}]$, and the scattering coefficient $b(\lambda)[m^{-1}]$.

The beam attenuation coefficient $c(\lambda)=a(\lambda)+b(\lambda)$ measures the exponential decay of a narrow laser beam due to either absorption or scattering. The single scattering albedo $\Lambda(\lambda)=b(\lambda)/c(\lambda)$ measures the portion of the beam attenuation which is due to scattering. The volume scattering function, $\beta(\lambda, \Theta)$ measures the angular distribution of the photon scattering.

The beam attenuation coefficient c is the primary indicator of the distance at which an EO imaging system will be able to deliver acceptable imagery. Frequently, the water clarity is characterized according to the range $R=1/c$ at which $cR=1$. Accordingly, when $1/c=2m$, for example, the water is said to be "2-meter water," and when $1/c=4m$, the water is said to be "4-meter water." Predictably, an imaging system will deliver acceptable imagery at a longer range — approximately twice as far — in "4-meter water" than it will in "2-meter water." The range R of an imaging system is frequently specified in terms of dimensionless beam attenuation lengths, where the range in beam attenuation lengths is given by the product cR . Thus, when an image is taken at a range where $cR=5$, the image is said to be taken at 5 (beam) attenuation lengths (AL).

The single scattering albedo Λ also plays a key role in the performance of EO imaging systems. In typical coastal waters Λ is 70-80 percent, although it can range from less than 50 percent to greater than 90 percent. When the albedo is low, attenuation by absorption is more predominant, leading to lower power levels. In this case, the imaging system is more likely to become power limited. In addition, blur/glow/forward scatter is less important when the albedo is low, so the image contrast is higher. On the other hand, when the albedo is high, blur/glow/forward scatter is more important, leading to a reduction in image resolution and contrast. In addition, attenuation due to absorption is less important, so the system performance is less likely to be power limited.

The volume scattering function (VSF) characterizes the angular dependence of the scattering, ranging from 0 degrees (forward) to 180 degrees (backward). The VSF affects all three of the primary mechanisms of image degradation. Backscatter depends on the magnitude of $\beta(\lambda, \Theta)$ near $\Theta=\pi$. Blur/glow/forward scatter depends on the magnitude of $\beta(\lambda, \Theta)$ near $\Theta=0$. Scattering at other angles contributes to attenuation.

Conventional underwater imaging systems, consisting of a video camera and floodlights, are limited to ranges of 1-1.5-beam attenuation lengths (the beam attenuation length in coastal waters is typically 1-2.5 meters) by backscatter noise. They lack the range and resolution required to facilitate rapid target identification.

The EOIDS Sensors project has evaluated laser-based imaging approaches capable of reducing the impact of environmental noise sources in order to facilitate rapid identification of MLCs in turbid littoral waters at useful ranges. Two approaches, laser line scan (LLS) and laser range-gated (LRG), have been evaluated in detail with the objective of extending the mine identification range to five or more beam attenuation lengths. LLS¹²³ systems reduce the effects of backscatter noise and blur/glow/forward scatter noise by synchronously scanning a narrow laser beam and a narrow field-of-view receiver across the sea bottom. Performance of LLS systems is dramatically superior to the performance of conventional imaging systems. LRG⁴ imaging systems (i.e., imaging LIDARs) perform significantly better than conventional systems because they reduce the impact of backscatter by temporarily "gating-out" much of the backscatter.

4. Testing of Laser-Based Underwater EO Imaging Systems

A test program was established in order to assess the relative merits of the LRG and LLS imaging approaches for SW/VSW mine identification. The cornerstone of this program was a sea test which provided simultaneous imagery with state-of-the-art LLS and LRG systems. This test provided the first direct, head-to-head, comparison of the performance of these two competing technologies. This test endeavored to remove all questions of unequal test conditions, since the two systems were imaging the same targets from the same platform through the same water at the same location at the same time.

The LRG system tested was Sparta Laser Systems Laboratory SEE-RAY LRG system. The SEE-RAY system employed a gated (approximately 8 nsec gate width), intensified CCD camera which generates images at standard video rates. F/85 receiver optics with a 29.4 mm aperture were employed which gave the system an instantaneous field-of-

view of 20 by 15 degrees. A tilt gimbal allowed movement of the system through an arc of 130 degrees across track, increasing the system field of regard. Laser illumination was provided by a 30 Hz, Q-switched, frequency doubled Nd:YAG laser operating at 532 nm with output power of approximately 100 mJ per 6 ns pulse. The laser output power could not be adjusted by the operator. However, zoom-optics on the laser allowed the output energy to be either distributed over the receiver field-of-view or concentrated near the center of the image. The gating range, camera gain, laser zoom, and gimbal tilt angle were controlled from an operator console. The raw LRG image data was displayed on a television monitor and simultaneously recorded on a 10 MHz, broadcast quality, U-Matic video recorder. After the test, digital snapshot imagery was generated from the video tape using an 8-bit digital frame grabbing board. Typically, bursts of approximately 20 sequential images were grabbed and visually inspected. The image deemed best was saved to hard disk for analysis. SEE-RAY is 39 inches long, 13 inches in diameter, and requires 500 watts of power.

The LLS system tested was the ART/SAIC LS-2048. The LS-2048 employed a CW argon ion laser with simultaneous output at 488 and 514.5 nm. Laser output power could be continuously adjusted from a maximum of 2 watts down to 65 mW in all laser lines. A rotating, four-faceted mirror and output optics assembly scanned the laser beam over a 70-degree section of the sea bottom while a synchronously rotating four-faceted mirror and input optics assembly focused the reflected light onto a photomultiplier tube receiver. The receiver circuitry incorporated a gated integrator which divided each 70-degree scan line into 2048 or 1024 pixels with an effective dynamic range of 12 bits. Raw, unprocessed, 12-bit data snapshot images of 1024 x 2048 pixels or 2048 x 1024 pixels were stored on hard disk for later analysis. Simultaneously, the scanned lines were processed as acquired and presented in a gray-scale waterfall display on the operator console. The continuous waterfall display was also recorded on S-VHS video tape. The LS-2048 is 80 inches long, 11 inches in diameter, and requires 5,000 watts of power.

In order to operate in SW during daylight hours, the LS-2048 was modified through the insertion of 3-nm pass band optical filters, centered at 514.5 nm, into the receiver optics. This improvement resulted in the first successful SW daylight imagery using an LLS. In addition, the filter rejected the LRG system's 532-nm laser light, allowing the LRG and LLS systems to simultaneously image the same targets. Of course, the 514.5-nm filter also rejected reflected light from the 488 line of the laser, resulting in an effective output laser power range (in the 514.5 line) from 800 mW down to 12 mW. The LLS laser powers reported in this document are the powers transmitted in the 514.5 line only.

The test platform chosen for this test was Applied Remote Technology's XP-21 autonomous undersea vehicle (AUV) operating in a tethered mode. A payload section and tether were fabricated which allowed the LRG and LLS sys-

tems to be simultaneously installed on the XP-21. The tether provided power to the imaging systems; command and control, and trickle power to the XP-21; and command and control and image pathways to and from the imaging systems. Use of the XP-21 allowed precise positioning of the imaging systems, repeatable test tracks, and very efficient data collection. The LRG systems performance was optimized through allowing its operating parameters to be adjusted to give the best image while the XP-21 hovered above each target. Data runs yielding simultaneous LRG and LLS imagery were typically executed only after the LRG parameters were optimized by hovering over each target.

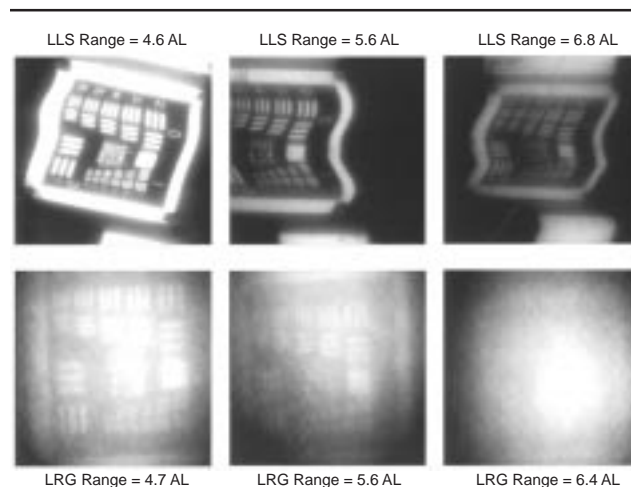
A shallow, turbid water environment was selected for the test. Periodic measurements of inherent and apparent optical properties of the water column were made throughout each test day. Parameters measured included the beam attenuation coefficient c , the absorption coefficient a , the diffuse attenuation coefficient k , and downwelling and upwelling irradiance.

Targets deployed included positive and negative contrast Air Force Resolution Targets. These targets were painted on 36-inch square aluminum panels using flat white and black paints with nominal reflectivities of 87 and 2 percent, respectively. The target designated as the “positive” target consisted of a white Air Force resolution pattern painted on a black background, while that designated as the “negative” target consisted of a black Air Force resolution pattern painted on a white background. This positive/negative target combination was selected to differentiate the effect of blur/glow/forward scatter from those of backscatter and attenuation by means of the following observations. First, notice that the inherent contrasts $C_{IN} = (White - Black) \div White$ of the positive and negative targets are identical, since they were prepared using the same paints on the same substrate material.⁵ Second, since attenuation reduces the observed signal from the positive (white) and negative (black) areas by the same factor A , it is seen that the observed contrast $C_{OBS} = ((A * White) - (A * Black)) \div (A * White) = C_{IN}$ cannot be reduced from the inherent contrast by attenuation.⁶ Third, since the same backscatter (BS) intensity is added to the white and the black areas, the observed contrasts $C_{OBS} = [(A * White + BS) - (A * Black + BS)] \div (A * White + BS) = (White - Black) \div (White + BS \div A) < C_{IN}$ are decreased from the inherent contrasts by backscatter. However, the contrast reduction due to backscatter (and attenuation) is identical for the positive and negative targets. Fourth, white areas lose intensity to black areas due to forward scattering, resulting in contrast reduction. Since negative targets have larger white areas, they are more susceptible to blur/glow/forward scatter noise, and therefore suffer greater contrast reductions. Accordingly, greater contrast reductions in negative targets are an indicator of the significance and magnitude of blur/glow/forward scatter effects on image quality.

Figures 1 and 2 present typical LLS and LRG images of the positive and negative Air Force Resolution Targets,

Figure 1

Positive (white) ranges for LLS versus LRG. LLS laser power was 190 mW.



respectively. The positive (white pattern on a black background) images in Figure 1 compare LLS pictures in the top row⁷ and with LRG images in the bottom row for comparable ranges as measured in beam attenuation lengths (ALs). The negative (black pattern on white background) images are similarly arrayed in Figure 2. Compare from top to bottom for LLS versus LRG contrast. These images show: (1) the LLS imagery is markedly superior to the LRG imagery for both the positive and negative targets; and (2) images of the bright background, negative targets are significantly poorer than images for the positive targets for both systems, but especially for the LRG system.

The superiority of the LLS imagery is not due to any purported power advantage. Laser power parity for the two systems, in terms of the same number of photons per pixel,

Figure 2

Negative (black) ranges for LLS versus LRG. LLS laser power was 190 mW.

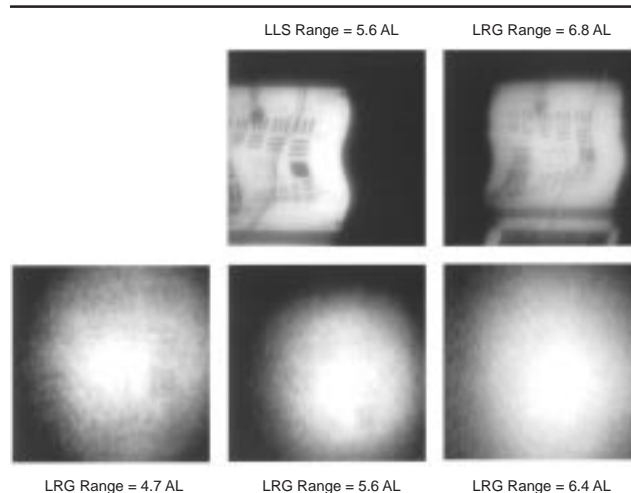
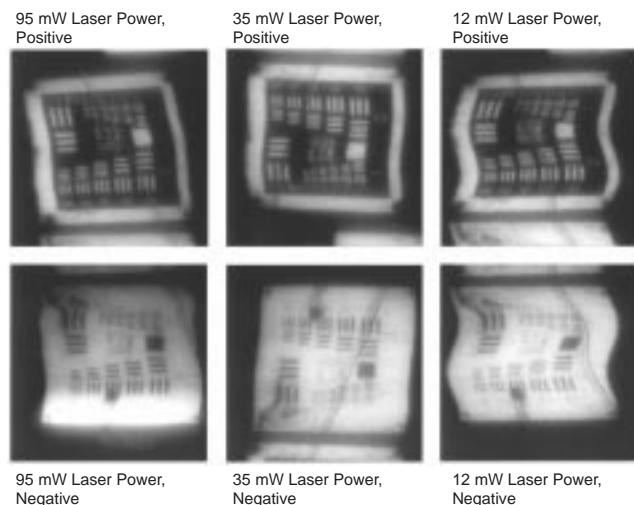
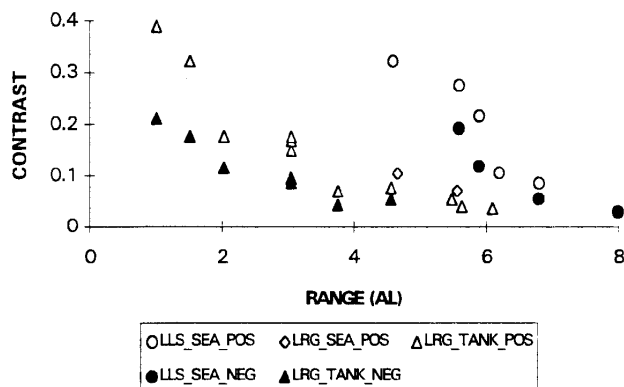


Figure 3
LLS imagery at 5.6 ALs at reduced laser powers.



occurred when the LLS power was approximately 200 mW. The LLS imagery in Figures 1 and 2 was taken at 190 mW laser power in the 514.5 nm laser line, yielding approximate energy parity with the LRG system. Figure 3 shows comparable LLS imagery taken at 5.6 ALs using 95, 35, and 12 mW laser power in the 514.5 laser line -- far below the energy density employed by the LRG system. Quantitative analysis reveals that the LLS contrasts are maintained at these low power levels, even though shot noise increases.⁷ Conversely, when the LRG system laser was "zoomed down" on the targets, resulting in an approximate four-fold increase in energy density on the target, there was no observable improvement in LRG image quality.

Figure 4
Contrast versus range plot for LLS and LRG images.



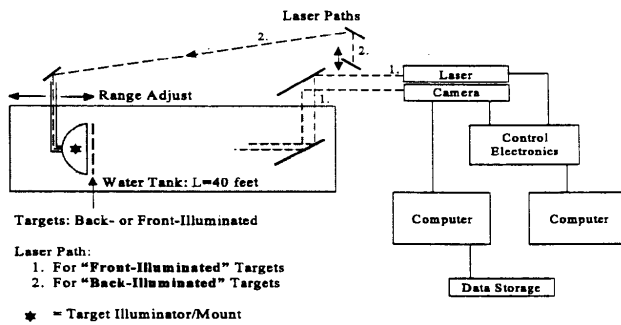
Contrast values were extracted from various three-bar patterns on these targets as a quantitative assessment of the relative quality of the images. Figure 4 presents these contrasts as extracted from the vertical three-bar pattern above the large square (e.g., the bar number 2 of series 0). The widths of these bars are 2.24 cm, while the sides of the large square are 10 cm. The sea test data has been supplemented with data from an earlier LRG tank test. Figure 4 shows the contrast points for the LRG and LLS systems are quite distinct and well separated. At any given range, the observed contrast of the LLS system is typically two to three times the contrast of the LRG system. Moreover, in order to match LLS contrasts, the LRG system frequently needed to be two or three times closer to the target.

The imagery and the contrast graph clearly show that the contrasts of the negative targets are significantly lower than the contrasts of the corresponding positive targets. As indicated above, this disparity between the positive and negative target contrasts cannot be explained by means of attenuation and backscatter. Rather, it is a direct indicator of the dominant role of blur/glow/ forward scatter noise in the degradation of the image quality. This dominant effect is particularly evident in the LRG system, where the negative target imagery is far inferior to the corresponding positive target imagery. For the LLS system, the negative target contrasts are smaller than, but still reasonably close to, the corresponding positive target contrasts, indicating success for the LLS system in partially rejecting blur/glow/forward scatter noise.

Even more direct evidence of the dominant role of blur/glow/forward scatter noise in the degradation of LRG imagery exists. Prior to the sea test, a test of a breadboard LRG system had been completed using a 4- x 4- x 90-foot test tank. The breadboard LRG was a dry unit; a large periscope was used to insert the laser pulse into the tank and to extract the return image pulse from the tank. This arrangement allowed data collection in a novel, "back-illuminated" configuration in addition to the normal "front-illuminated" configuration. In the back-illuminated configuration, backscatter noise was completely non-existent, allowing a very straightforward evaluation of the role of blur/glow/forward scatter noise in LRG systems. Figure 5 is a diagram of the tank test configuration showing the two laser paths. This test was conducted using fresh water, with Maalox used to add controlled amounts of turbidity to the water. Tests were conducted under simulated turbid, littoral water conditions, with beam attenuation lengths of 3, 2, 1, and 0.5 meters.

In the front-illuminated configuration (path 1), the laser beam is inserted into the water using a periscope and propagates through the water on its way to the target. The image pulse is reflected from the target, propagates through the water on its way back to the periscope, where it is extracted from the water and recorded on the gated camera. In this configuration, the image is degraded by all of the environmental noise sources; i.e., attenuation, backscatter and

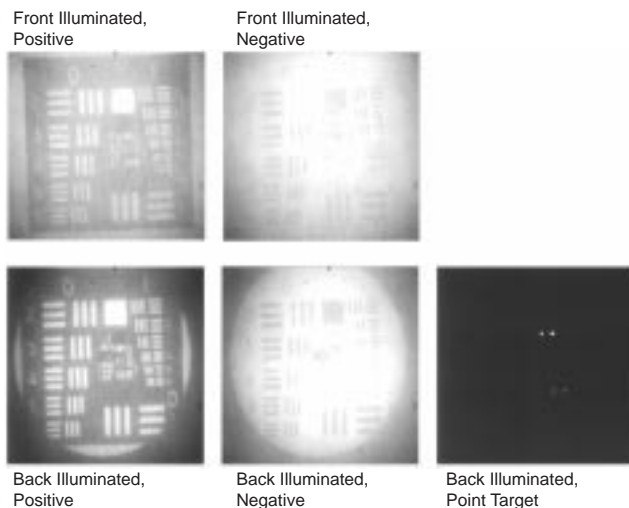
Figure 5
Test tank facility.



blur/glow/forward scatter noise. Contrast data from this configuration has been included in Figure 4.

In the back-illuminated configuration (path 2), the laser pulse propagates over the tank to the back side of the target, is inserted into the water by a second periscope, passes through a diffusion apparatus before back-illuminating transparent targets. In this configuration, backscatter noise is completely non-existent. In addition, the laser beam does not suffer attenuation due to scattering and absorption by water on its way to the target, so the intensity of the image leaving the target plane can be considerably higher than the corresponding image in the front-illuminated configuration. Accordingly, much of the back-illuminated imagery was collected in two modes. In the first mode, the laser pulse was attenuated so that the laser power leaving the target was approximately the same as the corresponding laser power in the front-illuminated configuration. In the second mode, the laser pulse was not attenuated, allowing an evaluation of

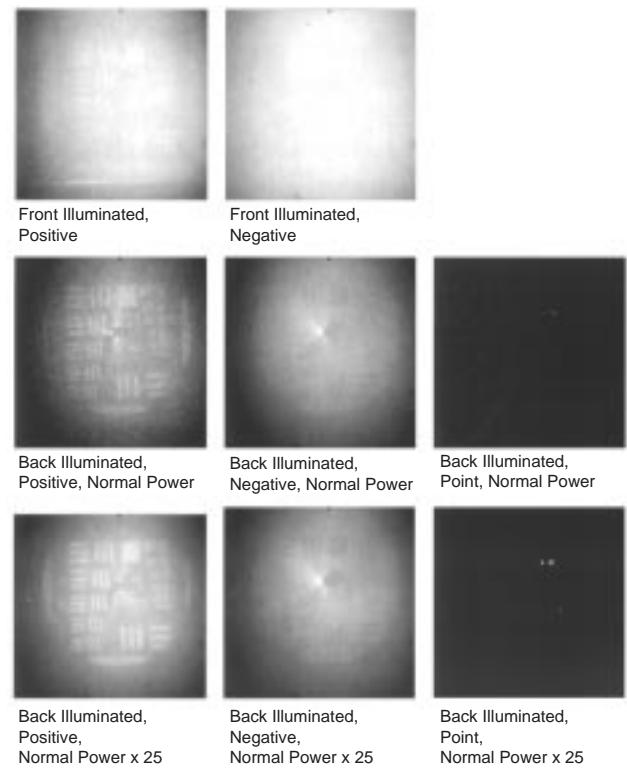
Figure 6
LRG tank test images, 3-beam ALs.



power-dependence of the image. Targets used in the back-illuminated configuration mode included positive and negative Air Force resolution patterns silk-screened on transparent plexiglass sheets, and a "point source" target. The point-source target consisted of six holes (diameters 8.33, 6.4, 4.0, 2.8, 2.0, and 1.0 mm) drilled in two rows (the two largest and the four smallest) in a sheet metal plate. The rows were separated by 232 mm, while the holes were separated by 51 mm.

Figures 6 and 7 show typical data sets from this tank test. Figure 6 illustrates LRG tank test data at a range of 3-beam attenuation lengths with front and rear illumination of

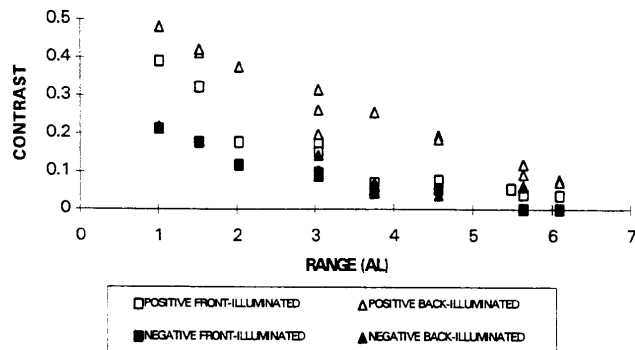
Figure 7
LRG tank test images 5.6-beam ALs, normal and high power.



the positive and negative targets. The outline of the 30-inch diameter "back-illumination spot" is clearly evident in the back-illuminated positive and negative target images. The lower right hand panel shows imagery of the back-illuminated "point-source" target. Figure 7 provides additional LRG tank test images at 5.6 ALs. The two top panels are standard front-illuminated, positive and negative targets. The panels in the middle line are back-illuminated, positive negative, and point targets, all at normal laser power. "Normal laser power" means that the back-illuminating laser power was attenuated to approximately match the laser power incident on the front-illuminated targets. (These powers were measured with a radiometer). The Figure 7 bottom three panels

Figure 8

Contrast versus range for LRG tank test.



are the same as the middle row, except that the back-illuminating laser power was not attenuated, yielding a laser power leaving the target significantly higher than the "normal laser power" leaving the front-illuminated, reflective targets. In this case the laser power was approximately 25 times higher than normal laser power.

Figure 8 presents contrasts extracted from this data for the front-illuminated, positive and negative Air Force Resolution Targets and corresponding back-illuminated positive and negative resolution targets for the back-illuminated targets. The contrasts of the back-illuminated targets are, as expected, higher than that of the corresponding front-illuminated targets. However, the contrast of the front-illuminated positive targets is significantly higher than the corresponding contrasts of the back-illuminated negative targets. This data places significant bounds on the magnitude of the contrast reduction due to backscatter; if the contrast reduction of the LRG system was mainly due to backscatter, the contrasts of the back-illuminated negative (and positive) targets should be significantly higher than the contrasts of the front-illuminated positive (and negative) targets. Moreover, the contrasts of the back-illuminated positive and negative targets should be close to identical. Neither of these is the case.

The data from the "point source" target clearly displays the fact that the LRG system was not power limited under the conditions of this test. The LRG system had enough sensitivity and gain to image the point source target at 5.6 ALs; it is blur/glow/forward scatter which limits the system performance, particularly for the negative targets. In fact, the system had enough sensitivity and gain to resolve the 8.33- and 6.4-mm point sources at 9-beam attenuation lengths. Under these conditions blur/glow/ forward scatter noise rendered even the positive back-illuminated image featureless.

It should also be noted that the LLS imagery and contrasts from the sea test is far superior to even the back-illu-

minated, enhanced power, LRG tank test imagery and contrasts.

Shortly after the completion of the sea test, a second, very brief, tank test was conducted which compared the performance of the LRG system in the sea test configuration with a prototype, enhanced receiver, LRG system. The prototype receiver has a higher quantum efficiency photocathode (approximately 45 percent versus approximately 15 percent) and a lower excess noise factor (approximately 1.1 versus approximately 3). However, these system improvements did not lead to significantly improved imagery under turbid littoral water conditions. In fact, under most conditions, the sea-test configuration performed at a par with, or superior to, the prototype configuration. Because this was a prototype receiver, special caution must be exercised when drawing conclusions. However, because the system was tested under turbid water conditions, the system was not power limited. Rather, its performance was limited by blur/glow/forward scatter noise, which was not addressed by these receiver enhancements.

The positive and negative Air Force Resolution Targets provide examples of imagery of high inherent contrast targets. Because of their high contrast, they are very cooperative targets. Caution must be exercised when extrapolating these results to imaging less cooperative, low inherent contrast targets.

5. Conclusions

This completed the first direct, head-to-head, performance comparison of LLS and LRG underwater imaging technologies. The results were an unambiguous appraisal of their relative merits for the mine identification mission in turbid, littoral waters. The following conclusions were reached:

The LRG system demonstrated: (a) successful detection (but not identification) of high contrast targets at relatively long range, (b) insensitivity to ambient light, and (c) insensitivity to platform motion. However, it had extreme difficulty identifying or even detecting low contrast targets even at relatively short ranges. It was found that the contrast and resolution required for the mine identification mission was severely limited by blur/glow/forward scatter noise.

The LLS system demonstrated the contrast and resolution required for mine identification under a robust set of conditions, including: (a) successful identification of high and low contrast targets, (b) successful imagery at high and low laser power, (c) successful imagery of tethered targets in the volume, and (d) successful imagery during day and night conditions. The system demonstrated effective reduction of blur/glow/forward scatter noise, as well as backscatter noise. Under certain situations, the LLS system became power limited, suggesting improvements in detector quan-

tum efficiency and increased laser power would be beneficial.

Based on these test results, requirements analysis, and sensor performance modeling, the decision has been made to base the LVIS sensor on LLS technology. The LVIS sensor has been designed, and is currently being fabricated by Applied Remote Technology. It is scheduled for initial sea testing in July/August 1995.

Biography

Michael Strand received a B. Chem. degree from the University of Minnesota, and a Ph.D. in Chemical Physics from the University of Chicago. He did postdoctoral research at the University of Colorado's Joint Institute for Laboratory Astrophysics from 1977 to 1980. He then taught in the physics and mathematics departments of Texas A&M University, before joining the staff of the Naval Surface Warfare Center, Coastal Systems Station in 1987. He is currently specializing in underwater laser-based imaging systems.

REFERENCES

1. J. Leatham and B. W. Coles, "Use of Laser Sensors for Search and Survey," *Underwater Intervention '93 Conference Proceedings*, 1993.
2. A. Gordon, "Underwater Laser Line Scan Technology," *Underwater Intervention '93 Conference Proceedings*, 1993.
3. T. J. Kulp, D. Garvis, and R. Kennedy, "Current Status of the NAVSEA Synchronous Scanning Laser-Imaging System," *SPE Proceedings*, Vol. 980, 1988.
4. B. A. Swartz, "Diver and ROV Deployable Laser Range Gated Underwater Imaging Systems," *Underwater Intervention '93 Conference Proceedings*, 1993.
5. Other definitions of contrast are possible, and may be more useful for certain purposes. This definition was used because it supports the separation of the effects of attenuation and backscatter from those of blur/glow/forward scatter.
6. Of course, if the signals are sufficiently attenuated, the image will be lost in the shot noise. Sufficient power and gain is required. However, shot noise is not the primary issue for the images under consideration.
7. The LLS images exhibit image distortions caused by non-uniform platform motions, especially roll induced by propeller torques when the platform is accelerating.
8. These images were taken during early evening, when ambient light levels were low. Comparable images taken near noon, when ambient light levels were

high, led to significant contrast reductions at the lowest laser power levels due to ambient light effects.

Advances in the Magnetic Detection and Classification of Sea Mines and Unexploded Ordnance

Ted R. Clem, Coastal Systems Station, Naval Surface Warfare Center, Dahlgren Division, Panama City, Florida

Abstract

Magnetic sensors offer a complementary approach to active acoustics for shallow water mine reconnaissance and hunting. The U.S. Navy has developed an approach using a 5-channel tensor magnetic gradiometer to provide enhanced classification and location in mobile operations beyond the capability offered by the commonly used single channel total field magnetometer. Buried mine detection and low false alarm rates were demonstrated using such a 5-channel gradiometer in fusion with acoustic sensors. This sensor featured bulk and wire niobium low critical temperature (low T_c) superconducting components cryocooled by liquid helium. Advances in material research and new concepts are being pursued to enhance opportunities with this 5-channel gradiometer concept: an advanced low T_c superconducting

prototype incorporating all thin film niobium superconducting components to demonstrate increased detection range in the Joint Countermine Advanced Concept Technology Demonstration, a high T_c superconducting concept using liquid nitrogen refrigeration to reduce package size and cryogenic support requirements, and a room temperature fluxgate prototype for man-portable applications where shorter detection ranges are useful. Recent experimental results using this technology have been obtained to demonstrate an enhanced capability for the detection of unexploded ordnance for environmental cleanup. In this paper, these recent advances in sensor development and the new testing results will be reviewed.

I. Introduction

Magnetic sensors have proven merit for mobile area surveys and search operations conducted from air, land or sea including application for the detection, classification, and localization of sea mines, unexploded ordnance (UXO), and chemical, biological and nuclear waste [1]-[4]. In fact, in an assessment conducted by the Jet Propulsion Laboratory for the Army Corps of Engineers, magnetic sensors in general were identified among the most useful sensors for UXO detection and localization, and superconducting gradiometers were specifically identified as the most useful tool in a class by themselves [5]. For applications in sea mine countermeasures, we can envision operational scenarios in which long-range detection is required for reconnaissance and hunting in preparation for an amphibious assault or shorter-range detection is required for diver mine detection and avoidance (Fig. 1).

In Sections I.A. and I.B., we shall describe two types of sensors which detect magnetic anomalies: sensors which detect changes in the local magnetic field, *magnetometers*; and sensors which measure the spatial derivatives of magnetic field, (*first order*) *gradiometers*.

A. Magnetometers

The performance of a magnetic sensor is measured by its detection range, which is a function of its configuration and sensitivity and the magnetic moments of the targets of interest. In the far field, a target can be well approximated as a magnetic dipole. In this approximation, relatively simple, analytic expressions can be written to relate sensitivity re-

quirements in terms of nominal values for target magnetic moment and range.

For the special case in which a circular, connected conducting loop with area A is carrying an electrical current I , we can define the magnetic moment of the loop as the vector $\mathbf{m} = IA\hat{\mathbf{n}}$ where $\hat{\mathbf{n}}$ is the normal to the loop in the direction defined by the right-hand rule for positive current. The International System (SI) unit for magnetic moment is ampere-meter-squared ($A\cdot m^2$). The magnetic induction variations in the Earth's field, without the use of very sophisticated for a magnetic dipole can be written as

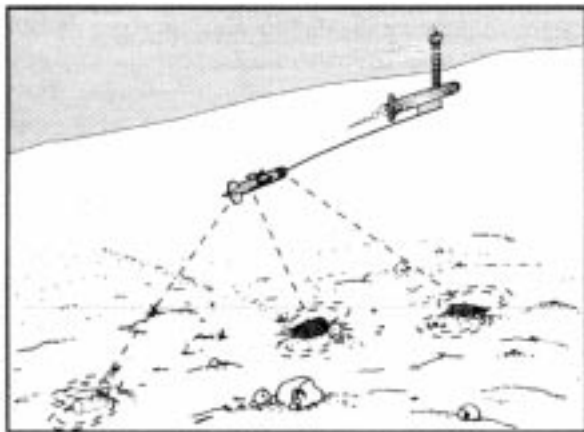
$$\mathbf{B} = \frac{\mu_0}{4\pi} \left[\frac{3(\mathbf{m} \cdot \mathbf{r})\mathbf{r}}{r^5} - \frac{\mathbf{m}}{r^3} \right] \quad (1)$$

The concept of magnetic moment \mathbf{m} can be generalized for an arbitrary magnetic body and the magnetic induction of the body will approach the result of (1) in the far field. In air, the magnetic induction \mathbf{B} is related to the magnetic field \mathbf{H} via $\mathbf{B} = \mu_0 \mathbf{H}$. Hereafter, \mathbf{B} will be used exclusively and will be referred to as the magnetic field. The following units for magnetic field will frequently be used to represent sensor sensitivities: nanotesla ($1 \text{ nT} = 10^{-9} \text{ T}$), picotesla ($1 \text{ pT} = 10^{-12} \text{ T}$), and femtotesla ($1 \text{ fT} = 10^{-15} \text{ T}$).

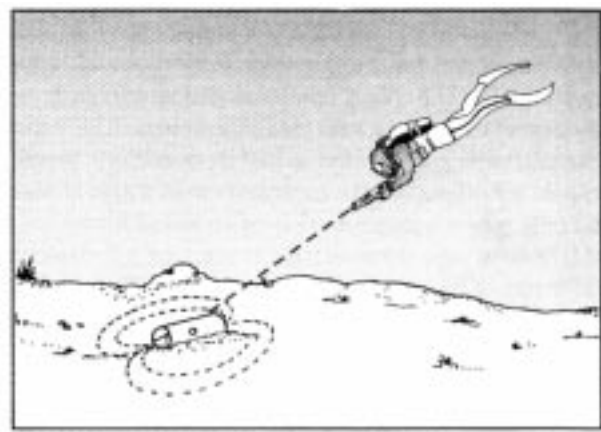
A number of sensors, notably fluxgate magnetometers and superconducting magnetometers, measure the individual vector components of field. A three-axis vector magnetometer, likely using fluxgate or superconducting sensors, is very useful for localization (providing three channels of information). For stationary applications in geophysics and barrier defense, such sensors are effective. However, to date, these sensor types have not proven effective for mobile applications, since means to compensate the anomalous signals aris-

Figure 1

Operational scenarios for the magnetic detection and classification in sea mine countermeasures: (a) operation onboard an unmanned underwater towed vehicle towed behind a semi-submersible remotely-operated vehicle for reconnaissance and hunting and (b) diver-portable operation for diver mine detection and mine avoidance.



(a)



(b)

ing from rotations in the Earth's magnetic field have not been devised.

Other magnetometers, notably those based on nuclear or atomic resonance processes, measure the magnitude of the total magnetic field and are known as total-field magnetometers. Let B_0 denote the magnetic field of the Earth, and let b denote the induction generated by an anomaly. If $|b| \ll |B_0|$, then the signal observed by a total field sensor (referenced to the baseline Earth field) is

$$b_m = |B_0 + b| - |B_0| = \sqrt{B_0^2 + 2B_0 \cdot b + b^2} - B_0 \approx \frac{B_0 \cdot b}{B_0} \quad (2)$$

As a result of the right-hand approximation above, a total-field magnetometer does not simply measure the magnitude of the magnetic-field anomaly, but measures instead the projection of that anomalous signal onto the earth's field

Total-field magnetometers have provided the generally accepted method for magnetic anomaly detection. In particular, the AN/ASQ-81 and its successor the AN/ASQ-208 are total-field magnetometers utilized by the U.S. Navy for submarine detection from airborne platforms. A major advantage of this type of sensor is its insensitivity to rotation in the Earth's background field of 50,000 nT (since total field is a rotational invariant).

Measurements by total field magnetometers are difficult to interpret because these sensors effectively measure the projection of the anomalous magnetic field vector onto the Earth's magnetic field instead of the total field. Interpretation often requires an experienced operator, and precise anomaly locations are difficult to obtain. Since total field magnetometers provide only one channel of information, they lack valuable target vector information. In particular, they

provide very limited localization and little capability for anomaly classification through moment determination. Moreover, these sensors are limited in field operation to sensitivities at levels approaching 0.1 nT as a result of geomagnetic noise, i.e., temporal variations in the Earth's field, without the use of very sophisticated compensation schemes.

B. Gradiometers

The gradient of the magnetic field (in standard MKS units of T/m) is a second-order tensor with components given in Ref. 6 by

$$G_{ij} \equiv \frac{\partial B_i}{\partial x_j} = -\frac{3}{r^7} \frac{\mu_c}{4\pi} \left\{ m \cdot r (r_i r_j - r^2 \delta_{ij}) - r^2 (r_i m_j + r_j m_i) \right\} \quad (3)$$

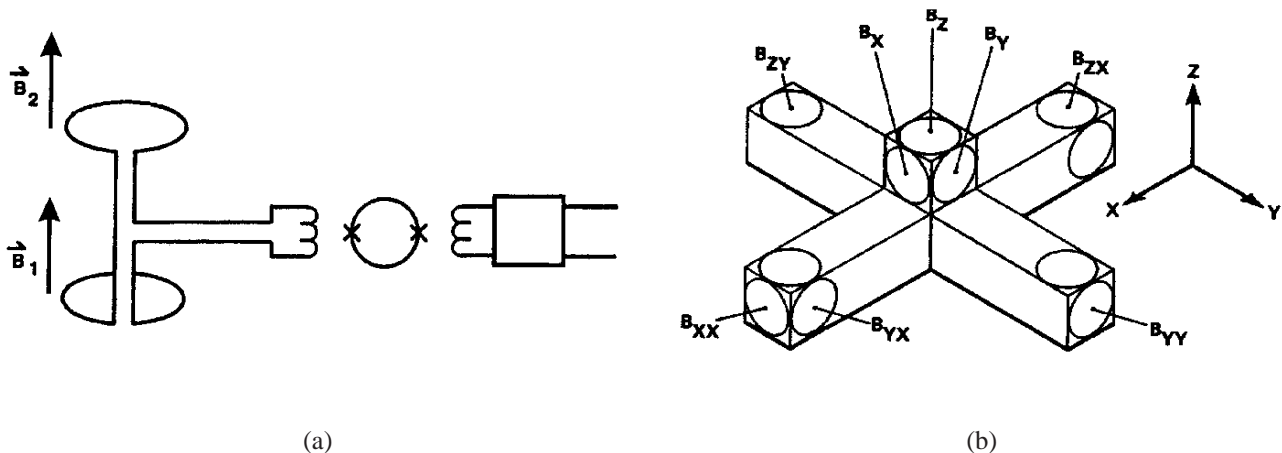
As a result of Maxwell's equations in free space, only 5 of these 9 tensor elements are independent. For this reason, (first order) gradiometers are typically designed with 5 independent gradient channels, using the minimum number which permits characterization of the local tensor gradient field.

It is feasible to determine the bearing vector and the magnetic-moment vector direction of the dipole by inversion of the gradient equations at a single point only [6]. More recently it has been shown that the addition of gradient rate information at a single point leads to a unique solution for dipole position and moment vector [7].

The contradiction of the gradient tensor defined by

Figure 2

Gradiometer sensor concepts including (a) a single SQUID-based gradiometer channel and (b) a conceptually simple 5-channel gradiometer configuration capable of magnetic dipole localization and moment classification (with 3 orthogonal magnetometers for motion compensation).



$$G \equiv \sqrt{\sum_{i=1}^3 \sum_{j=1}^3 G_{ij} G_{ij}} \quad (4)$$

is a rotational invariant associated with the gradient tensor analogous to the magnitude of the field vector. This quantity may prove very useful for applications in which a gradiometer is subjected to large rotations during the period of measurement, e.g., hand-held operation (in contrast to straight runs onboard stabilized platforms) [6].

An example of one configuration to measure a single-gradient tensor component and a simple configuration to measure 5 independent gradient components are displayed in Figure 2. Each gradient tensor component is measured by a spatially separated loop pair connected in a common-mode rejection configuration. 3 vector magnetometers are included in the 5-channel gradiometer displayed in Figure 2(b) to compensate for the residual magnetometer signals in the gradiometer channels that arise as a result of manufacturing imperfections in the gradiometer loops.

Gradiometers offer the potential to remove many of the limitations associated with magnetometers because the output of a gradiometer is typically produced by twin magnetometers operating in differential mode. In particular, this configuration provides common-mode rejection of the nominal 0.1-nT temporal variations in the Earth's field and of the nominal 1000-nT field changes arising from typical 1 degree sensor rotations while in towed motion.

Gradiometers may be fabricated using many available magnetometer technologies. Available fluxgate and total-field magnetometers can perform at levels approaching 1-10 pT, while superconducting magnetometers utilizing Superconducting Quantum Interference Devices (SQUIDs) can perform at levels on the order of 1-10 fT. The extreme perfor-

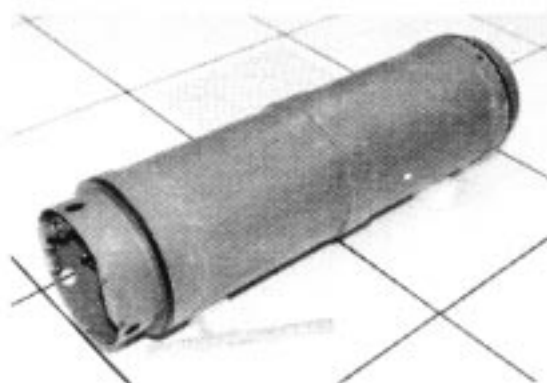
mance available from superconducting magnetometers provides a capability to fabricate gradiometers with high sensitivity having short baselines. The short baseline provides a compact package with extreme coherence between the magnetometers. The coherence is required to maintain high performance when in motion, and the compact package is amenable to implementation aboard one vehicle. In addition, with the compact sizes, a large number of gradient channels can be integrated into a small package to obtain complete position and moment determination of a magnetic dipole target at a single point in space.

C. The Superconducting Gradiometer/Magnetometer Sensor

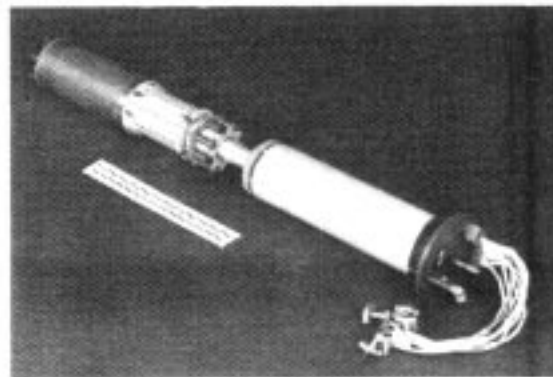
Almost all of the efforts with SQUID sensor technology have dealt with sensors inside a very controlled laboratory environment, and to a more limited extent outside the laboratory at stationary locations, notably for geophysical measurements. During the 1980's, the Coastal Systems Station (CSS) developed the Superconducting Gradiometer/Magnetometer Sensor (SGMS) specifically for mobile operations outside the laboratory environment (Fig. 3). The sensor employs largely niobium bulk and wire superconducting technology (with thin-film Josephson Junctions), features dc SQUIDs housed inside superconducting shields, and is convectively cooled to 4 degrees Kelvin by helium gas evaporating from a liquid helium reservoir. Under some field conditions, the SGMS has attained sensitivities on the order of 1pT/m-Hz^{1/2} at 0.1 Hz. In comparison total-field gradiometers (with a 0.3-meter baseline) specifically designed for operation onboard a moving platform have achieved sensi-

Figure 3

Major subassemblies in the SGMS package: (a) dewar and (b) sensor probe unit.



(a)



(b)

tivities on the order of $30 \text{ pT/m-Hz}^{1/2}$ at 0.1 Hz and a fluxgate gradiometer described in Section VII.A has achieved a sensitivity on the order of $300 \text{ pT/m-Hz}^{1/2}$ at 0.1 Hz [1], [2].

The CSS initiated the Magnetic and Acoustic Detection of Mines (MADOM) Project starting in 1985. This project successfully demonstrated the value of magnetic and acoustic sensor fusion for mine reconnaissance and hunting. The SGMS demonstrated, for the first time, high sensitivity and rugged, robust, and reliable performance of a superconducting gradiometer operating outside the laboratory environment onboard a towed underwater vehicle with sea testing conducted for a period of 7 years. Gradiometer operation was automated (with the exception of semi-automated initial tuning) and fully-automated, real-time magnetic detection and classification signal processing was demonstrated to provide effective and accurate moment determination and localization for single and multi-target cases [1], [2].

D. Quantitative Comparison of Magnetometers and Gradiometers

The signal strength of a magnetic dipole decreases as the third power of the range for magnetic fields and as the fourth power of the range for magnetic field gradients. The approximate ranges of magnetometers and gradiometers are displayed in Figure 4 as functions of dipole strength and sensor sensitivity. It can be shown that the sensitivity requirements for a magnetometer and a gradiometer, respectively, to have the same detection range r against a given dipole target, is given by the approximate relation $N_g/N_m \sim 3/r$. For

Figure 4

Approximate ranges (in meters) of magnetometers and gradiometers as a function of target strength in terms of magnetic moment (in units of A-m^2). Curves are given for different sensor sensitivities (in units of nT for magnetometers and nT/m for gradiometers assuming a 10 dB signal-to-noise ratio in both cases).

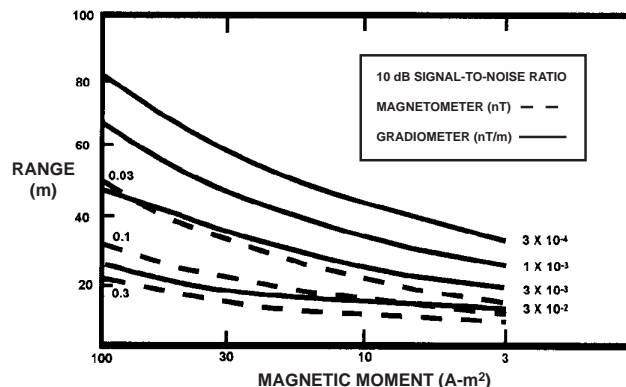
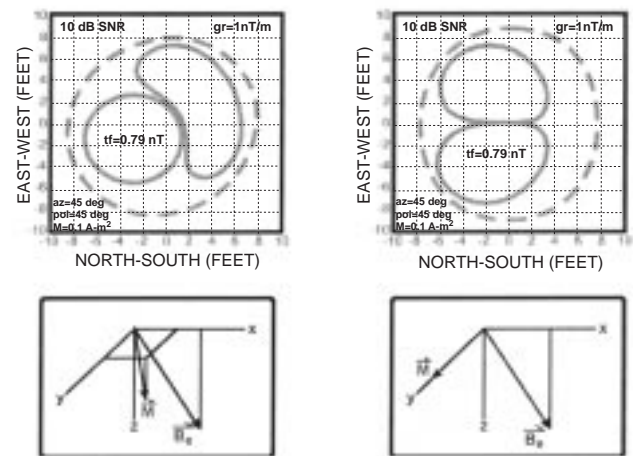


Figure 5

A comparison of magnetometer and gradiometer capabilities for target localization. The profiles measure tf = total field (Equation (2)) and gr = gradient magnitude (Equation (4)). Profiles are given for a magnetic dipole centered at origin with (a) a general orientation and (b) orientation in an east-west direction. Observe that the gradiometer profiles are approximately circularly symmetric about the dipole's location so that "gradient" searches normal to the gradient magnitude profiles are meaningful for the gradiometer. In contrast, the magnetometer profiles are not amenable to such straightforward interpretation.



example, the detection of a mortar shell with a magnetic moment of 0.1 A-m^2 at a range of 3 m , requires a magnetometer with sensitivity of 0.36 nT or a gradiometer with sensitivity of 0.36 nT/m (given a 10-dB signal-to-noise ratio for both cases).

It should be noted that the high rate of signal reduction with the fourth power of distance in the case of a gradiometer represents an apparent shortcoming for a gradiometer configuration. We believe that the ability to develop gradiometers with sensitivity greater than $1 \times 10^{-3} \text{ nT/m}$ for mobile operations and the extreme difficulty in utilizing magnetometers with sensitivity greater than 0.1 nT in mobile operations significantly outweighs this shortcoming. Moreover, the fourth power reduction of detection range with moment for a gradiometer has merit for the detection of targets with relatively small moments. For example, a 3 pT/m gradiometer can detect an individual 500-pound bomb (with a moment of 30 A-m^2) at a range of 33 m and a 60-mm mortar shell (with a moment of 0.1 A-m^2) at a range of 8 m . Hence there is only a factor of approximately 4 reduction in detection range for a 60-mm mortar shell compared to the 500-pound bomb although there is a factor of 300 in reduction of magnetic moment.

An example of the ease of interpretation for 5-channel gradiometer data compared to single-channel total-field magnetometer data is displayed in Figure 5. Magnetic profiles have been generated for a 60-mm mortar shell buried 1

meter under ground for two different orientations with respect to the Earth's background field. In this example, the magnetometer profiles and gradiometer profiles are given by the anomalous total field, Eq. (2), and the corresponding changes in magnitude of the gradient tensor, Eq. (4), respectively. The complex total field profiles require precision data and critical interpretation to localize dipole sources. The symmetric gradiometer profile leads to straightforward interpretation convenient for gradient searches for dipole localization.

II. Scenarios for Gradiometer Mobile Operation

We can envision three general types of operational scenarios: relatively long-range rapid surveys for target clusters, more moderate-range searches against individual targets, and detailed close-in surveys. The selection of magnetic sensor type will largely depend on these operational requirements, determined primarily by the desired detection range, which is, in turn, a function of the magnetic moment of the targets and of sensor sensitivity. The selection also depends on such factors as financial budgets, logistical support and technical expertise of the operators. To date, mag-

netic sensor approaches have provided limited localization and mapping capabilities. To gain widespread acceptance, approaches must be introduced which provide accurate localization and target classification, and which lend themselves to straightforward interpretation and minimal training. Performance must not be limited by magnetic noise from the host platform and other subsystems. For land-based operations, the system must be capable of operating over rough, overgrown terrain. The sensor and associated signal processing also must deal effectively with environmental noise.

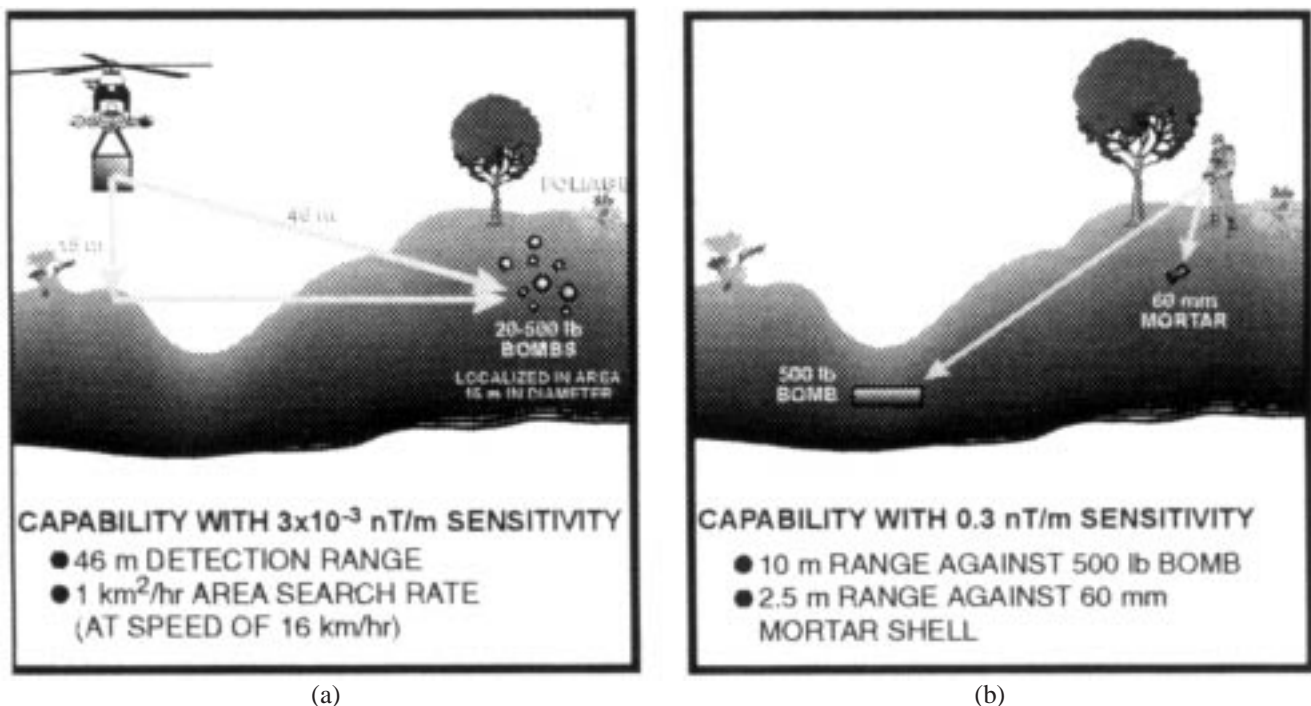
A. General Considerations

Long-range rapid surveys conducted from an aircraft have been proposed for initial surveys to locate clusters of UXO targets [4]. The mine reconnaissance/hunting demonstration of MADOM represents an example of a moderate-range search. Land-based manual surveys or diver operations for mine detection or avoidance provide examples of close-in surveys. High sensitivity will be critical for the long-range and moderate-range scenarios, but such sensitivity will likely be sacrificed for the close-in surveys at ground level. In fact, local geologic noise limits a gradiometer's noise floor to levels on the order of 0.05 up to 10 nT/m-Hz^{1/2} which may limit the use of high-sensitivity gradiometers such as the SGMS for some land-based operations.

A perspective on the role of higher sensitivity gradi-

Figure 6

Two modes of operation for 5-gradient channel sensors: (a) wide-area surveys using high sensitivity sensors and (b) short-range searches for single targets using less sensitive sensors.



ometers used for wide-area searches and lower sensitivity gradiometers for close-in surveys can be obtained from the following example (Fig. 6). A 3 pT/m gradiometer can detect a grouping of twenty 500-pound bombs (clustered in a circle several meters in diameter) at a range of 46 meters. An area search rate of 1 km²/hr can be obtained when the sensor's altitude is 15 meters moving at a forward speed of 15 km/hr. When deployed from the ground, a less sensitive 300 pT/m gradiometer would provide detection ranges of 10 meters and 3 meters for the detection of a 500-pound bomb and a 60-mm mortar shell, respectively.

Two fundamental approaches for operation of a 5-channel tensor gradiometer stand out. First it will often be convenient to conduct straight-line searches at constant velocity for airborne and underwater vehicle operation and also for some land-based surveys if the terrain admits straight-line trajectories. For other cases, including many man-portable land-based and diver operations, it will be unreasonable to expect controlled operator motions along straight-line trajectories at constant velocities. In either case, we can implement signal processing using point-by-point inversion of the motion-compensated gradiometer signals. For the special case of straight-line searches, we can also utilize least-squares fit to the time series in order to improve target detection. One approach using point-by-point inversion is described in Section II.B and one approach using a least-squares fit is described in Section II.C below.

B. Localization using Point-by-Point Signal Inversion

As mentioned above, the five independent gradient tensor components at a single point can be used to construct the bearing vector to a dipole source, and a scaled moment vector with the same direction as the dipole moment vector and a magnitude given by m/r^3 [6]. The difficulty with this inversion is that there are multiple solutions: two nontrivially related solutions in a given half space, and two additional solutions obtained by reflection of the first two through an origin centered on the gradiometer. This multiplicity of solutions has limited the practical application of this algorithm. More recently, Wynn [7] has investigated the use of the rate of change of the gradient tensor components, and their role in resolving the scaling and uniqueness issues associated with the gradient tensor inversion.

For a sensor with specified translational velocity v , the time rate of change of the gradient tensor components has the form

$$G_{ij} = \frac{3\mu_0}{4\pi r^5} \{ 35(m \cdot r)(v \cdot r)r_i r_j - 5r^2[(m \cdot v)r_i r_j + (m \cdot r)(v_i r_j + v_j r_i) + (v \cdot r)(m_i r_j + m_j r_i) + (m \cdot r)(v \cdot r)\delta_{ij}] + r^4[m_i v_j + m_j v_i + (m \cdot v)\delta_{ij}] \} \quad (5)$$

These equations have been inverted to give multiple solutions for the bearing vector and a scaled moment vector in the direction of the dipole moment vector with a magnitude given by m/r^5 . The solution for bearing vector and moment vector direction common to the two inversions is unique, and the different scaling for the scaled moments in the two inversions yields the range to the dipole, resulting in a unique solution for m and r on a point-by-point basis. In practice, it is not necessary to specify a sensor velocity. All that is needed is knowledge of the position of the gradiometer relative to the Earth's reference frame. Work is ongoing to apply these algorithms to the practical interactive localization of buried UXO by means of a man-portable tensor gradiometer.

C. Localization using a Time-Series Least-Squares Fit

A mathematical model for detection, classification, and localization (D/C/L) of multiple stationary magnetic dipole targets using a gradiometer (with 5 independent tensor gradiometer channels appropriately selected and 3 orthogonal magnetometer channels) moving in a straight line trajectory past the targets at a constant speed has been developed and validated in the MADOM project. The 5 output signals $S_i(t)$ ($i=1,2,\dots,5$) from the 5 independent gradiometer channels and the 3 magnetic field components $B_l(t)$ ($l=1,2,3$) are measured as a function of time as the sensor moves past the targets. The time derivatives of field $dB_l(t)/dt$ are calculated from the $B_l(t)$ for eddy-current compensation. The objective of this model is to extract the dipole signals $G_{ij}^{(k)}(t)$ ($k=1,2,\dots,n$) for the unknown number n of dipole targets and then to determine the magnetic moments and the positions of the n targets.

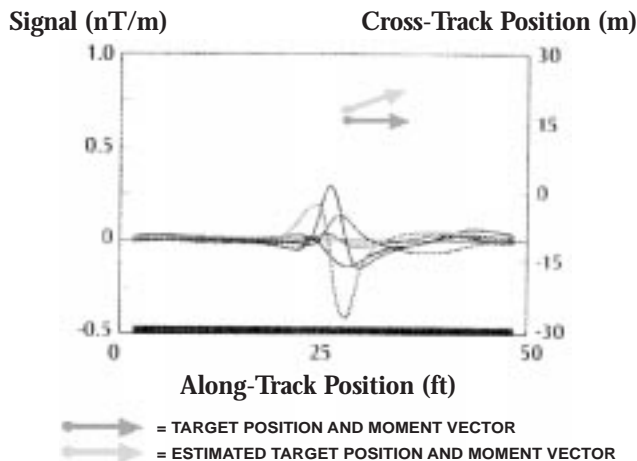
The model describes the signals S_i in the 5 gradiometer channels by the equations

$$S_i(t) = \sum_{j=1}^5 c_{ij} \left\{ \sum_{k=1}^n G_{ij}^{(k)}(t) \right\} + \alpha_i + \sum_{l=1}^3 \beta_{il} B_l(t) + \sum_{l=1}^3 \gamma_{il} \dot{B}_l(t) + v_i(t) \quad (6)$$

where c is the pre-determined calibration matrix for the gradiometer, $v_i(t)$ and α_i are uncompensated noise (setting the noise floor of the channel compensation parameters per channel) and channel biases, respectively, and β_{il} and γ_{il} are the balance and eddy-current vectors for channel i . An iterative analysis first estimates the α 's, β 's, γ 's, (a total of 35 parameters) and then executes a gradient search for the location of the single target that best fits the residual signal. The α 's, β 's, γ 's, and target location and moment are then optimized, and the procedure is repeated for a second target. Targets continue to be added until finally no target can be found whose signal contributes substantially to a reduction

Figure 7

The five gradiometer signals in a 45-m section of data on a pass near a Mk83 1000-lb bomb.



in total signal power, at which point the algorithm terminates.

Fig. 7 displays the motion-compensated signals obtained from the gradiometer and the information extracted from the algorithm in detecting a 1000-lb Mk83 bomb. The five gradiometer signals are displayed for a 45-m section of data with the bomb located 15 m to port and 5 m below the gradiometer at the closest point of approach. The measured and predicted target location, moment, and orientation are also displayed to indicate the capability of the algorithm to provide good fits to the data.

III. Mobile Underwater Debris Survey System

A project has been initiated to develop and evaluate a Mobile Underwater Debris Survey System (MUDSS) capable of finding and accurately mapping the locations of UXO ranging from small shells to large bombs in water depths of from 4 to approximately 100 feet in coastal regions at formally used defense sites [3]. The effort involves a collaboration between CSS and the Jet Propulsion Laboratory [8]. In addition to the application of UXO detection at coastal sites utilizing underwater towed sensor suites as described in this section, the use of a superconducting gradiometer in a system concept for rapid airborne reconnaissance and survey of UXO sites has been proposed [4].

A. General Project Description

The MUDSS project is divided into two phases. Phase I, which ran for one year and culminated in an at-sea feasibility demonstration of a multi-sensor MUDSS prototype against UXO in a drill target field. The feasibility demonstration was successfully executed in August and September of 1995 in St. Andrews Bay (near Panama City, FL) with the SGMS utilized for magnetic detection. Phase II will culminate in 1997 in a technology demonstration consisting of a UXO survey at a yet-to-be-determined formally used defense site.

Figure 8 depicts the first version of the MUDSS system which was fielded in 1995 for the feasibility demonstration. The surface craft is a custom designed magnetically and acoustically quiet, shallow draft, trailerable catamaran.

Figure 8

The Mobile Underwater Debris Survey System: (a) artist's concept detailing key features of the system and (b) photograph of system in transit to test site with the dead-weight depressor housed out of water for speed and maneuverability.

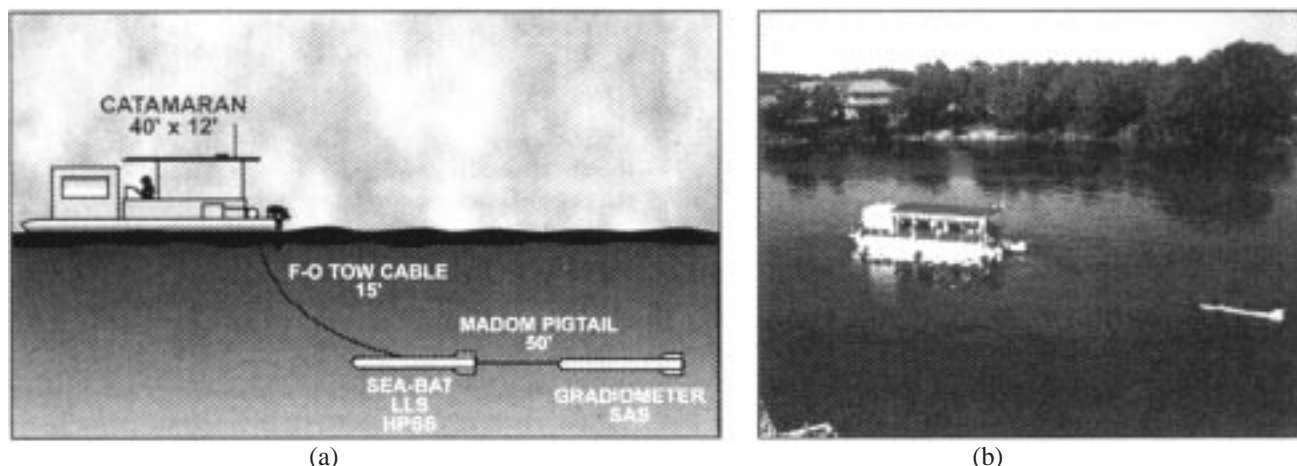
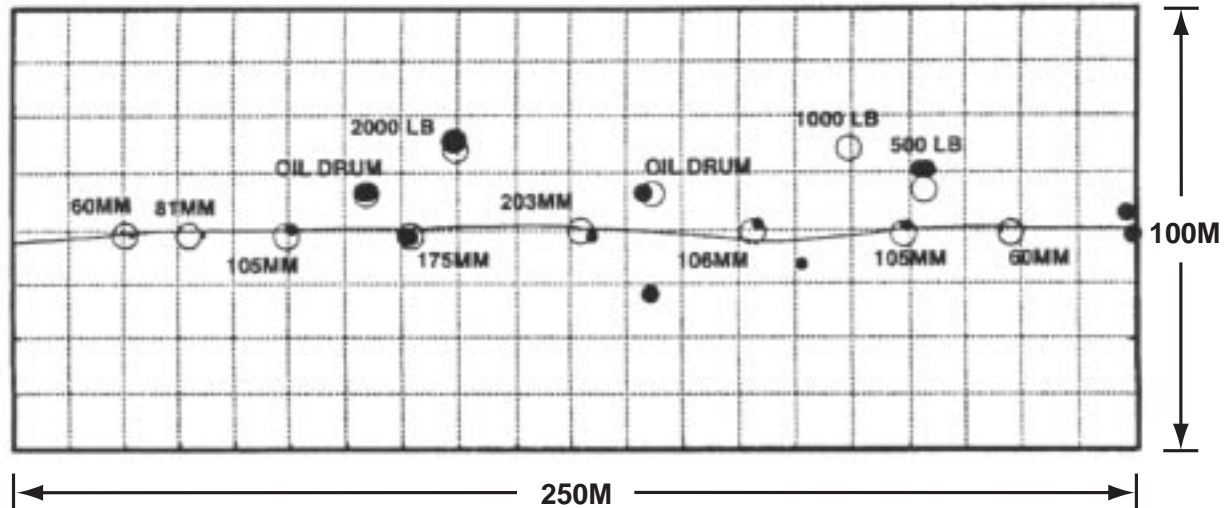


Figure 9

Gradiometer targets found in one run over the linear field with the open circles \circ indicating the actual target locations and the solid circles \bullet indicating the positions predicted by the D/C/L algorithm. The size of the solid circles \bullet indicates the predicted magnitude of the target's magnetic moment.



A dead-weight depressor is suspended off of the back of the catamaran to maintain the appropriate depth for sensor operation and to house part of the sensor suite (a RESON Seabat ahead looking sonar, a CSS-developed high frequency sidescan sonar, and a Raytheon-leased LS 4096 laser linescanning electro-optic sensor). A second neutrally buoyant tow body trailing the deadweight depressor houses a CSS-developed low frequency synthetic aperture sonar and the SGMS.

Reference 3 gives a detailed description of the feasibility demonstration test field layout, the testing procedures, and the performance of the acoustic and electro-optic sensors. Specific details relevant to the gradiometer demonstration are given here.

B. Gradiometer Results from the Feasibility Demonstration

A linear target field was laid out to evaluate the SGMS performance. The field consisted of a row 200 m in length of eight small and medium-sized targets (mortar and artillery shells ranging in caliber from 60 up to 203 mm) running north-south; a second shorter row of three medium-sized targets (two oil drums and a Mk82 500-lb bomb) parallel to, and 9 m east of, the first row; and a third row of two targets (a Mk83 1000-lb bomb and a Mk84 2000-lb bomb) 9 m east of the second row. A marker and a sonar calibration panel with ferrous anchors were laid at one end of the linear field. Estimates of the magnetic moments for the targets obtained

from the D/C/L algorithm described in Section II.C are tabulated in Table I. These magnetic moments ranged from 0.03 A-m² for one 60mm mortar shell up to 120 A-m² for the 2000-lb bomb.

The detection range for these targets is also tabulated in Table I. Absolute range is given for a gradiometer with sensitivity of 3 pT/m-Hz^{1/2} at 0.1 Hz assuming a 10 dB signal-to-noise ratio and relative range is given for fixed gradient sensitivity (normalized to 1 for a 60mm shell with magnetic moment of 0.03 A-m²). Observe that the 2000-lb bomb is detectable at 8 times the range of the 60mm mortar shell.

The predicted results from the D/C/L algorithm to estimate location and to classify the targets according to mag-

TABLE I
ESTIMATES OF MAGNETIC MOMENT FOR THE UXO TARGETS

Target	Moment (A-m ²)	Range (m)	Relative Range
60mm shell	0.03 - 0.2	6 - 9	1-1.5
81mm shell	0.3	10	1.6
105mm shell	0.7	13	2.2
175mm shell	3	18	3
203mm shell	5	22	3.6
55 gal oil drum	10 - 25	27 - 32	4.5 - 5.3
500-lb bomb	20	30	5
1000-lb bomb	40	36	6
2000-lb bomb	120	48	8

netic moment are displayed in Fig. 9 for one pass of the system through the target field. Open circles designate the actual location of the targets, while the solid circles indicate the predicted positions. The size of the solid circles indicates the magnitude of the targets' magnetic moment. For the feasibility demonstration, the nominal performance of the gradiometer channels was on the order of $3 \text{ pT/m-Hz}^{1/2}$ at 0.1 Hz . The D/C/L algorithm was effective in localization and classification (by moment magnitude) all of the targets in this pass with the exception of the 1000-lb Mk83 bomb. This exception provides an example of multi-target localization for which there are 2 targets (the 500-lb bomb and the 105mm shell) in this data window in addition to the 1000-lb bomb. In this case the algorithm successfully localized the 500-lb bomb and the 105mm shell with high signal strength, but failed to localize the more distant 1000-lb bomb with a relatively weak signal strength. The ferrous anchors for the marker and calibration panel at the right hand side of the map and two clutter objects in proximity to the 106mm shell (not a part of the target set) were also detected during this run. Double detections are displayed in Figure 9 for two targets, the 500-lb bomb and one of the two oil drums. These represent target detections by the D/C/L algorithm in two separate data segments. The high degree of overlap for the double detections is suggestive of the degree of accuracy obtained with this algorithm.

IV. Clutter Rejection

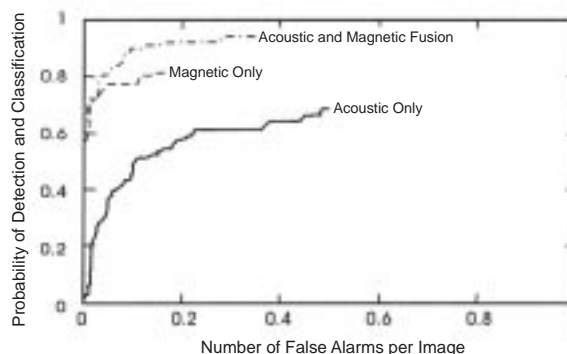
Generally active acoustic approaches have proven to be an effective means to detect, classify and localize tethered sea mines or bottom mines proud with respect to the bottom in deeper waters. However the shallow-water bottom mine environment is an especially difficult acoustic environment in which to operate. Interfering reverberations from the air/sea and sea/bottom interfaces, bottom topographical features, general harbor debris, and mine burial present a difficult acoustic environment for bottom mine detection. In coastal regions, the density of debris clutter may

TABLE II
FEATURES USED TO TRAIN THE NEURAL NETWORK DEVELOPED IN [10]

Magnetic Features	Acoustic Features
Total magnetic moment	Average signal-to-noise ratio (SNR) over object's length
Y-component of moment	Average SNR over object's width
Z-component of moment	Maximum of the ratio of SNR for length to SNR for width
Depth estimate	Number of intense pixels
Confidence level for correct object classification and localization	Target length
	Target width
	Estimated clutter density

Figure 10

The probability of detection and classification for acoustic and magnetic sensors alone and for neural-network fusion data from both sensors given as a function of the number of false alarms per image in the two tracks from 10 to 27 meters on either side of the vehicle.



lead to a high false-alarm rate using conventional imaging sonar approaches alone.

For effective clutter rejection, it is very desirable to use distinctly different sensor approaches. The application of two or more collocated sensors operating simultaneously has the potential to reduce false alarms and provide robust detection in a wide variety of background conditions. For mine reconnaissance and hunting, the combination of magnetic sensors with sonars provides such an alternative. In the MADOM sea testing, more than 90% of the acoustically mine-like clutter was not magnetically mine-like.

Several investigations have been conducted recently using automated neural network approaches to assess the merit of magnetic and acoustic data fusion [9], [10]. The following result was obtained courtesy of L. Smedley and G. Dobeck [10]. A set, consisting of 215 sonar images containing an assortment of drill targets and clutter objects, was assembled using data collected from sea tests with the SGMS and the MADOM low frequency synthetic aperture sonar. For each sonar image, the magnetic detections were co-registered. An attractor-based k-nearest neighbor neural network was developed using the magnetic and acoustic features given in Table II.

Receiver operating curves (ROCs) for this data were established for different detection ranges, recognizing the fact that the two sensors are effective over different ranges. The ROC for the individual sensors and for the two-sensor data fusion (obtained from this neural network) are displayed in Fig. 10 for tracks on both sides of the vehicle in a range where both sensors were effective. For these tracks, there were 93 drill targets in the 215 images.

We observe in this figure the improved detection and classification obtained using the data fusion. For an accept-

able rate of 0.1 false alarms per image, the probability of detection and classification was 0.5 for the acoustic sensor alone and 0.77 for the magnetic sensor alone. The probability of detection and classification increased to 0.9 for a rate of 0.1 false alarms per image using this neural-network data fusion. Although these results were taken from a small data set of 215 images, we believe that the trend clearly demonstrates the substantial benefit of magnetic and acoustic data fusion for shallow water mine reconnaissance and UXO survey.

V. The Thin-Film Gradiometer

We believe that the current technology, represented by the SGMS sensor, is reaching its performance limit. This technology is largely characterized by the use of bulk and wire niobium (Nb) superconducting components. Advances in Nb thin film technology to obtain increased low frequency sensitivity and the relative simplicity of the thin-film processing in contrast to labor-intensive assembly of bulk SQUID packages and the hand winding of wire loops are appealing. For mobile applications, the greater intrinsic balance, i.e., common-mode rejection of the Earth's magnetic field, obtained from thin-film lithography compared to manual winding of wire loops and the removal of bulk magnetic components, including superconducting diamagnetic components such as shield canisters, is important to reduce anomalous signals in the gradiometer sense loops arising from acceleration-induced relative motion of parts. A project to develop a high sensitivity, all thin-film gradiometer sensor for mobile deployment is being pursued by the CSS, IBM Research [11], Ball Aerospace [12], Lockheed-Martin [13],

Quantum Magnetics [14], and the Naval Research Laboratory [15] for demonstration in the Joint Countermine Advanced Concept Technology Demonstration.

A. Cryogenic and Room-Temperature Electronics

Major advances in Nb thin-film fabrication technology has led to the development, for the first time, of high quality low frequency SQUID based magnetic sensors utilizing Nb-AlO_x-Nb tri-layer technology on a 5" scale. This work has led to the production of totally unshielded gradiometers which have been successfully demonstrated to operate in the Earth's magnetic field.

A cryogenic probe assembly for high performance in mobile operation has been manufactured with 3 tensor gradiometer circuits mounted on a single-crystal silicon rod and mounted to the dewar neck plug (Fig. 11). The gradiometer circuits consist of 2 counterwound magnetometer loops, each 3.8 cm square with a baseline of 5.3 cm, monolithically coupled to the SQUID. The precision lithography in conjunction with a configuration in which the sense loops, the SQUID washers, and their modulation and feedback coils are all patterned as gradiometers has provided extreme balance in order to maintain full sensitivity in the presence of field changes on the order of 1000 nT.

A benchtop version of high frequency flux-lock loop (FLL) feedback electronics with a modulation frequency of 16 MHz, a factor of 15 to 30 times the current frequency available with commercial electronics, has been developed in order to assure specified signal-to-noise ratios required from the all thin-film gradiometer channels (using air-core thin-film output transformers in place of wire-wound ferrous-core transformers) and to provide a high bandwidth for electromagnetic interference immunity [16].

B. The Advanced Liquid Helium Dewar

A dewar prototype, referred to as the Advanced Liquid Helium Dewar, was developed to assure that the dewar would not limit sensor performance (Fig. 12). A flexible design approach supported by detailed thermal, mechanical and field calculations was pursued. Stringent material selection and magnetic screening standards were established. The materials typically were chosen to be as magnetically clean as possible, with residual magnetizations 10 orders of magnitude smaller than that for soft steel. The magnetic gradient stability and the eddy current stability are 100 times better than the preceding state-of-the-art established with the SGMS.

An exchange gas cooling approach was pursued in place of the convective cooling utilized in the SGMS dewar.

Figure 11
The TFG Cryogenic Probe Assembly.

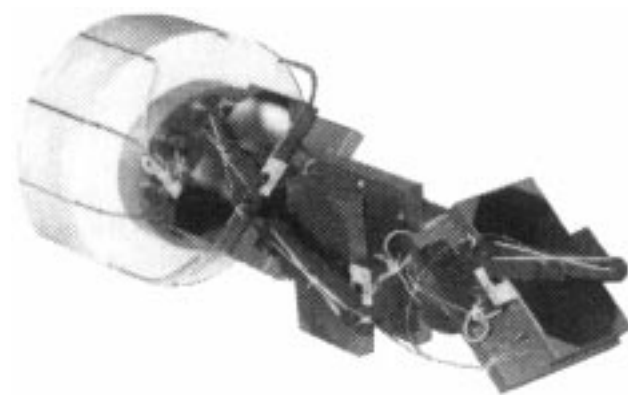


Figure 12

The Advanced Liquid Helium Dewar.



New innovations for thermal management have been implemented - anti-slosh baffles, thermal filters to isolate sensor area from bath temperature fluctuations, aluminized-mylar-blankets for radiation shielding custom etched to reduce the eddy currents, and thermal networks of 99.999% pure aluminum wire for temperature uniformity. Temperature stability in motions typical of tow operations is on the order of $1 \mu\text{K}/\text{Hz}^{1/2}$ at 0.1 Hz a factor three orders of magnitude better than for the SGMS dewar [17].

C. Field Testing of the Integrated Sensor

The integrated sensor prototype has been evaluated recently under field conditions. For this testing, the benchtop room temperature FLL electronics (which have a significant magnetic signature) are operated off a 15-m cable outside the test facility (remotely positioned some 13 m away from the sensor so as not to limit the performance of the sensor in motion). Stationary measurements have been conducted in this test setup in order to establish a baseline for the motion testing; i.e., to quantify any deterioration of performance in motion. In this configuration for the sensor, white noise on the order of $50 \text{ fT}/\text{m}\cdot\text{Hz}^{1/2}$ ($10 \mu\Phi_0/\text{Hz}^{1/2}$) has been demonstrated. The knee for 1/f noise occurred at approximately 1 Hz and the noise floor rose to approximately $200 \text{ fT}/\text{m}\cdot\text{Hz}^{1/2}$ ($40 \mu\Phi_0/\text{Hz}^{1/2}$) at 0.1 Hz. The nominal balance of the gradiometers is estimated at $1 \times 10^4/\text{m}$ (as measured indirectly from a comparison of compensated and uncompensated motion spectra obtained in preliminary motion testing), a factor of at least 20 greater than obtained with the wire-wound SGMS loops without the trimming procedures required for wire loops. The dynamic range of the gradiometers is 6×10^6 .

For comparison, these electronics evaluated in a labo-

ratory environment (integrated with a preliminary version of the gradiometer circuit currently being evaluated) operating off a 2-m cable has white noise on the order of $4 \mu\Phi_0/\text{Hz}^{1/2}$ with about 1/3 of the noise from the preamplifier. The knee for 1/f noise also occurred at approximately 1 Hz and the noise floor rose to approximately $7 \mu\Phi_0/\text{Hz}^{1/2}$ at 0.1 Hz. The electronics demonstrated a very high closed loop bandwidth exceeding 2.5 MHz and a very high slew rate greater than $1 \times 10^6 \Phi_0/\text{sec}$ at frequencies up to 1 MHz [16]. In comparison, the SGMS has a bandwidth of 100 kHz and a slew rate of $2.5 \times 10^4 \Phi_0/\text{sec}$.

D. Development of a Field-Deployable TFG

The existing TFG is being upgraded to a ruggedized field-deployable version. A fully-populated 5-channel cryogenic probe assembly is being developed to replace the 3-channel laboratory unit. A compact field-deployable room-temperature electronics package is being developed to replace the benchtop FLL electronics currently utilized for the laboratory version and to provide automated sensor control signal digitization, and data linking. Miniaturization of the electronics into a single integrated unit mounted onto the sensor (as required to obtain sensitivity of the integrated sensor in motion) represents a major undertaking. The entire analog and digital electronics for 5 gradiometer and 3 magnetometer channels is being packaged into a unit 43 cm in diameter and 56 cm in length. The package must have magnetic signature consistent with the sensitivity requirements in motion, power reduced by a factor of 30 compared to the laboratory prototype, and dimensions to minimize the length of the sensor body section for underwater deployment as much as possible. Production is in progress with final assembly and testing to be completed in 1997 for integration in an underwater tow system for mine hunting, specifically for demonstration in the Joint Countermine Advanced Concept Technology Demonstration, and for UXO surveys.

VI. High T_c Superconducting Technology

As a result of nitrogen cooling, the development of sensors utilizing the high- T_c materials with nitrogen cooling provides an opportunity for significant size reduction, an ease of maintainability and convenience in comparison to the low- T_c technology with helium cooling, factors critical to gain widespread acceptance of the superconducting technology over other magnetic sensor approaches.

A. Perspective on Nitrogen Cooling for Naval Operations

A broad-based assessment of refrigeration technology including liquid, solid, and triple-point nitrogen dewars and active cryocoolers was conducted [1], [18]. The conclusion from this assessment is that liquid nitrogen dewars represent the best choice for near-term development of a high performance high T_c superconducting gradiometer for mobile applications. The design for an open (vented) liquid nitrogen dewar with dimensions 45 to 75 cm in length and 30 to 50 cm in diameter has been established consistent with sensitivity goals (Fig. 13). These dimensions are consistent with available space in underwater tow bodies of interest for U.S. Navy applications. A final choice for dimensions in any final dewar design would be based on a tradeoff between space and hold time. Results of the concept analysis indicate that a dewar with dimensions of 43 cm in diameter and 75 cm in length would have a hold time of approximately 33 days. This hold time is over 6 times greater than the hold time for the Advanced Liquid Helium Dewar which has the same diameter but is 150 cm long, twice the length of the nitrogen dewar.

The benefits for naval mobile applications which can be obtained from these reduced cryogen requirements include: (1) a significant reduction in down time during operations; (2) affiliated reductions or elimination in labor requirements for cryogen support during critical phases of an operation; (3) reduced failures in the cryogenic circuits or in the dewar (such failures typically occur during cryogen recycling); and (4) the elimination of an additional footprint on ship deck required for helium storage. In addition, the

use of liquid nitrogen in place of liquid helium significantly reduces supply logistics as a result of the wide availability of nitrogen on the market at domestic and most foreign ports and the availability of a large number of liquifiers in the U.S. Fleet, with at least 54 units identified. Significant cost savings are expected from reduced costs for cryogen supply.

B. Device Development under this Project

Since 1993, there have been a number of laboratory results reported on magnetometer prototypes with white noise better than $200 \text{ fT/Hz}^{1/2}$. A number of test samples, magnetometer circuits and gradiometer circuits have been developed in conjunction with this project. This included a report of $26 \text{ fT/Hz}^{1/2}$ at 1 Hz for a 2×2 -cm magnetometer [19]. As an element of this program, the impact of flux trapping for unshielded operation of high T_c sensors in the Earth's magnetic field has been investigated and identified to be more problematic than for the corresponding low T_c niobium thin-film sensors. Approaches are being pursued to circumvent current limitations in high T_c fabrication technology [20]-[24]. In particular, the three-sensor gradiometer approach described in Section VII.B is an example of one means to circumvent these limitations. In that approach, magnetic-field coils are utilized to null out the Earth's magnetic field at the sensing circuit. The field nulling significantly reduces noise associated with non-ideal magnetization effects in the high- T_c superconducting material.

C. 3-Axis High T_c Magnetometer for Stationary Applications

A 3-axis magnetometer prototype developed by Conductus under a SBIR contract has been evaluated (Fig. 14). This sensor is being developed for stationary operation with a focus on geophysical applications. Results obtained to date are very promising. The sensor has been operated in the field totally unshielded without any deteriorated performance compared to its performance shielded. Magnetometer performance of $140 \text{ fT/Hz}^{1/2}$ at 1 Hz has been demonstrated under stationary field conditions. This performance is a factor over 50 times better than the performance obtained from the best commercial fluxgate magnetometers. The 3 High- T_c SQUID magnetometer circuits in this unit have been working reliably for over one year without failure [25].

Figure 13

Liquid nitrogen dewar concept with design versatile for multiple applications. This dewar has an outer diameter of 43 cm (17") (compatible with operation in a 53-cm (21") vehicle) and a length of 75 cm (30"). The dewar is projected to have a hold time of 33 days.

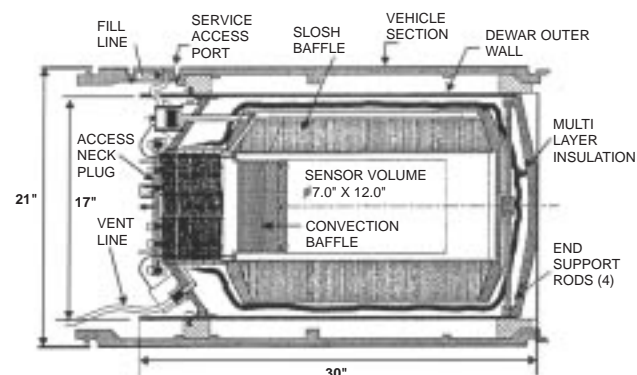


Figure 14
3-channel high- T_c magnetometer.

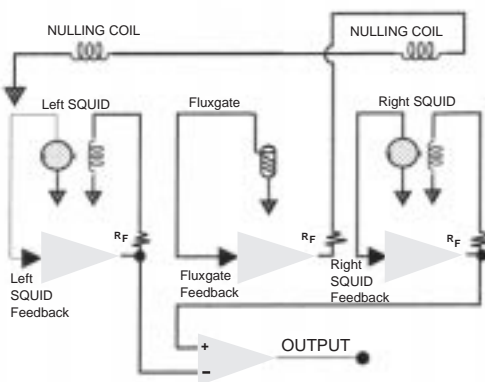


VII. The Three-Sensor Gradiometer

One advantage of the niobium-based superconducting technology, especially for mobile operation, is the ability to fabricate large scale counter-wound gradiometer sense loops using either niobium wire or multi-layer thin films with cross-overs. This allows signal subtraction using very low-noise passive circuits prior to signal processing with active amplifier circuits, which greatly reduces dynamic range requirements from the active electronics. A gradiometer can be configured using two independent magnetometers with signal

Figure 15
The three-sensor gradiometer concept for one case in which there are two primary high T_c SQUID-based magnetometers and a third fluxgate magnetometer for field nulling.

THREE SENSOR GRADIOMETER (TSG)



subtraction performed at the output of the two magnetometers. The CSS pursued this approach in the early 1970's using fluxgate technology. Good stationary performance was obtained at that time, but there was insufficient dynamic range in the processing of the differential signals to operate the sensor in motion.

In order to circumvent this dynamic-range limitation arising by differencing two individual magnetometer signals during mobile operation, a novel approach patented by IBM Research is being pursued [26], [27]. A third magnetometer is used for common mode rejection, feeding back a signal to the two primary magnetometers which nulls out the ambient background field. This concept is denoted as the three-sensor gradiometer (TSG). The concept is depicted in Fig. 15 for one case in which there are two primary high T_c SQUID-based magnetometers and a third fluxgate magnetometer for field nulling.

A. The Fluxgate Version of the TFG

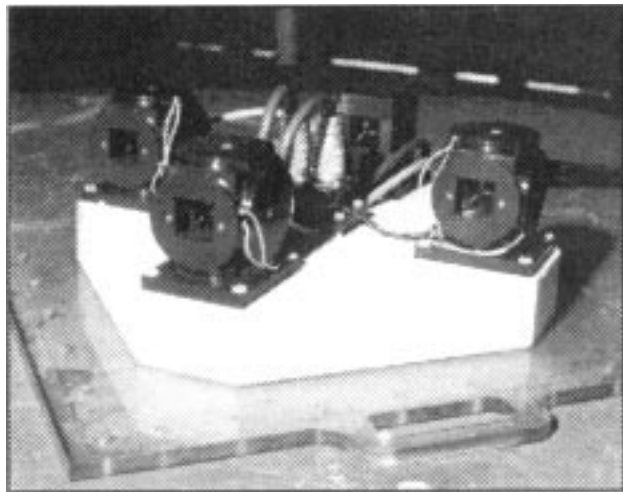
The basic TSG concept has been successfully pursued using room temperature fluxgate magnetometers (in place of the SQUID magnetometers). A laboratory prototype of the fluxgate TSG has been developed and demonstrated (Fig. 16). This sensor features four commercial 3-axis triad sets of fluxgate magnetometers in a planar square array with a one-foot diagonal baseline. One triad set of fluxgate magnetometers serves as a reference to measure the 3 mean magnetic field vector components at the array. The remaining three sensor triads are each mounted inside their own 3-axis Helmholtz coil sets which null the mean magnetic field at the sensor triad. The residual signals at the triads are processed through their commercial electronics and appropriate combinations are subtracted via differential amplifiers. In this manner, 6 tensor gradient terms can be calculated of which 5 are independent. In the laboratory prototype, analog electronics are utilized to implement the magnetic feedback currents with manual feedback adjustments determined to an accuracy of 5 decimals by a digital signal-processing routine. Sensitivity better than 0.3 nT/m at 0.1 Hz in motion has been demonstrated [28], [29].

A Phase I SBIR has recently been awarded to Quantum Magnetics to develop a ruggedized field-deployable version designed to improve the performance of the laboratory prototype. This version will be compact and light weight for man-portable operation. It will feature an integrated computer for fully automated sensor control and signal processing and a display to provide the operator easy target detection, classification, and localization.

This sensor offers the opportunity to become the mainstay for man-portable magnetic surveys, replacing the total field magnetometer by offering unambiguous detection, moment classification, and localization. Although its range

Figure 16

Laboratory prototype of a 5-channel fluxgate gradiometer utilizing the three-sensor gradiometer concept.



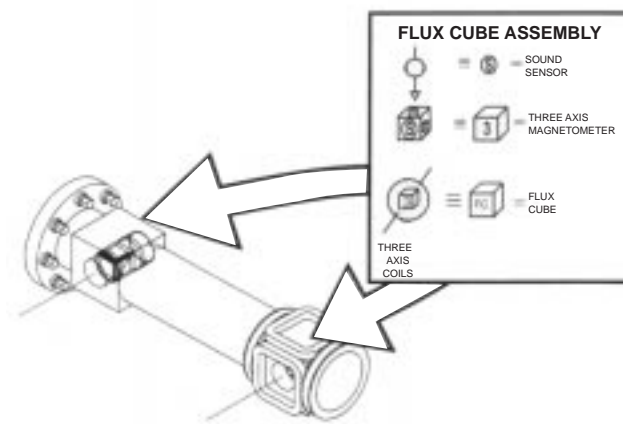
will be limited by factors of 4 to 10 compared to the superconducting gradiometers described previously, this type of sensor will provide a low cost approach convenient for many applications and will avoid a need for cryogenics.

B. The High T_c Version of the TFG

A project to develop and to demonstrate feasibility of a compact field-deployable high- T_c superconducting gradiometer concept for mobile operation is being pursued by the CSS, IBM Research, Ball Aerospace, Quantum Magnetics,

Figure 17

Concept for the laboratory prototype of a 3-channel high- T_c superconducting gradiometer utilizing the three-sensor gradiometer concept.



the Naval Research Laboratory, and Lockheed-Martin. As mentioned previously, it has been possible to fabricate high-sensitivity gradiometers in niobium technology by using monolithic wire or thin-film counterwound sense loops. Neither wire or thin-film monolithic loops can currently be manufactured using the high- T_c technology to provide the higher sensitivities in motion offered by niobium technology. A high- T_c gradiometer preliminary design has been established based on the TSG concept and its performance in motion has been modeled. The TSG approach circumvents the current limitations in high T_c manufacturing technology, providing long baselines by using normal metal wire to connect the two SQUID magnetometers.

Further improvement in performance is expected using the high T_c SQUID magnetometers in place of fluxgate magnetometers as a result of their intrinsically greater sensitivity. A laboratory test article is being developed to evaluate this concept (Fig. 17). This test article incorporates two flux cubes with each flux cube consisting of 3 orthogonal high- T_c SQUID-based magnetometers with dimensions of 1 cm². The two cubes, separated by a baseline of approximately 30 cm, permits the synthesis of 3 tensor gradient components. For this test article, a 3-axis fluxgate triad is used to provide the 3 reference channels required in the feedback loop to null out the mean ambient background field. This high T_c gradiometer is expected to surpass significantly the motion performance of any conventional non-superconducting magnetic sensor technology and is projected to have sensitivity better than that of the low- T_c SGMS.

Conclusions and Summary

Magnetic sensors provide one tool valuable for mobile search operations and surveys for targets with a significant magnetic signature. Superconducting SQUID-based sensors theoretically represent the most sensitive of known magnetic sensors. SQUID-based magnetometers have been demonstrated with sensitivities on the order of 1 fT/Hz^{1/2} at frequencies down to 0.1 Hz, while fluxgate and total-field magnetometers are demonstrating sensitivities down to 1-10 pT/Hz^{1/2} at 0.1 Hz.

The U.S. Navy has developed the Superconducting Gradiometer/Magnetometer Sensor, a superconducting gradiometer which has provided long-range detection compared to conventional non-superconducting magnetic sensors. This sensor has been utilized to demonstrate a capability for buried mine detection and clutter rejection. As a result of the multi-channel approach, the sensor provides an accurate localization capability and multi-target discrimination. The magnetic detection-and-classification signal processing developed in conjunction with the sensor has proven to be effective, providing a fully automated, real time capability. This

high-tech sensor has provided reliable, rugged performance in undersea tows conducted over a period of seven years. The sensor has been operated in the same tow vehicle adjacent to a sonar without a loss in performance. This technology is available off-the-shelf to provide the greatest capability for magnetic detection and localization ever demonstrated. Work has continued recently with this sensor under the MUDSS Project to demonstrate its utility for UXO survey.

A new approach incorporating all thin-film niobium components is being pursued for greater detection range in mobile operation. A laboratory prototype is being evaluated with white noise on the order of $50 \text{ fT/m-Hz}^{1/2}$ rising to approximately $200 \text{ fT/m-Hz}^{1/2}$ at 0.1 Hz under stationary field conditions. A field deployable version is under development to be utilized in the Joint Countermine Advanced Concept Technology Demonstration in 1998.

It is only a matter of time before high- T_c devices will be available with performance comparable to that which has already been demonstrated with low- T_c devices. Magnetometer performance of $140 \text{ fT/Hz}^{1/2}$ at 1 Hz has been demonstrated under stationary field conditions. This performance is a factor over 50 times better than the performance obtained from the best commercial fluxgate magnetometers. The benefits in reduced size, longer hold times, and reduced logistics and support make the high- T_c approach attractive compared to its low- T_c counterpart.

The localization capability afforded by 5-channel gradiometers (and not previously afforded by conventional magnetic sensors) is expected to add impetus to the acceptance of magnetics for mobile applications. The development of a 5-channel fluxgate gradiometer is currently in progress. Sensitivity better than 0.3 nT/m at 0.1 Hz in motion has been demonstrated.

As a result of a much lower cost and no special support requirements, such sensors will likely be sold in larger numbers for short-range applications. Their wider usage would then enhance the opportunity to display the utility of the greater classification and localization capability afforded by the 5-channel approach. With greater acceptance of the 5-channel approach, end users will likely want to obtain sensors with greater sensitivity. It is likely that the eventual development of high-performance, reliable high- T_c gradiometers will work synergistically with an increased acceptance of the more powerful magnetic signal-processing approaches. Hopefully, the time scales for this supply and demand will be commensurate and so expedite sensor developmental efforts.

Acknowledgments

This work was supported by the U.S. Office of Naval Research, the U.S. Strategic Environmental Research and Development Program, and the U.S. Small Business Innovative Research Program. Among the many individuals who

supported these developments at the CSS, the author acknowledges the contributions from G. I. Allen, G. Dobeck, M. C. Froelich, J. D. Lathrop, D. J. Overway, J. W. Purpula, L. Smedley, L. Vaizer, R. F. Wiegert, and W. M. Wynn. Finally the CSS would like to acknowledge the contributions from IBM Research, Ball Aerospace, Conductus, Quantum Magnetics, Lockheed Martin Federal Systems, the Naval Research Laboratory, and the Jet Propulsion laboratory including the more recent individual efforts from R. H. Koch, J. Rozen, J. H. Eraker, J. M. Schmidt, R. Cantor, P. V. Czipott, D. K. Lathrop, D. Gambrel, and R. J. Soulen, Jr.

Biography

Dr. Ted Clem joined the research staff at the Naval Surface Warfare Center (NSWC) Coastal Systems Station (CSS) in 1982. His research interests include superconducting sensor design and investigation of noise mechanisms associated with superconducting materials. The Chief of Naval Research awarded him for co-authoring the Best Navy Independent Research Paper in 1989. In addition, he received the CSS's Award for Special Achievement in Science and Technology in 1985 for his endeavors to understand important noise sources in superconducting sensor technology and in 1989 for research with the high temperature superconducting materials. He is also coordinator of low frequency applications in superconductivity for the Naval Consortium for Superconductivity. He is a member of the American Physical Society. Currently he manages the CSS's Superconducting Gradiometers Project.

REFERENCES

1. T. Clem, "Nitrogen Cooled Superconducting Gradiometers for Mine Reconnaissance from Small Underwater Vehicles" in the *Proceedings of the Symposium on Autonomous Vehicles in Mine Countermeasures*, pp. 6.91-6.102, April 1995.
2. T. Clem, "Superconducting Magnetic Sensors for Mine Detection and Classification," in *Detection Technology for Mines and Minelike Targets*, Dubey, A.C., Cindrich I., Ralston, M. and Rigans, K., (eds.), the International Society for Optical Engineering, pp. 374- 383, April 1995.
3. J.D. Lathrop, J.F. McCormick, P.J. Bernstein, J.T. Bono, D.J. Overway, G.S. Sammelmann, T.H. Chao, and K.C. Scott, "Mobile Underwater Debris Survey System (MUDSS) Feasibility Demonstration report," in *UXO Forum 1996 Conference Proceedings*, PRC Environmental Management Inc., pp. 427-436, April 1996.
4. D.C. Summey and G.J. KeKelis, "Fused airborne sensor technology," in *Detection and Remediation*

- Technologies for Mines and Minelike Targets*, A.C. Dubey, R.L. Banard, C.J. Lowe, and J.E. McFee, Eds., the International Society for Optical Engineering, Proc. SPIE 2765, pp. 226-232, April 1996.
5. Jet Propulsion Laboratory Sensor Technology Assessment for Ordnance and Explosive Waste Detection and Location, JPL Report D-11367 Revision A, 1994.
 6. W.M. Wynn, C.P. Frahm, P.J. Carroll, R.H. Clark, J. Wellhoner, and M. J. Wynn, "Advanced Superconducting Gradiometer/Magnetometer Arrays and a Novel Signal Processing Technique," IEEE Trans. on Magn., Vol. MAG-11, pp. 701-707, March 1975.
 7. W.M. Wynn, Magnetic Dipole Localization using the Gradient Rate Tensor Measured by a Five-Axis Gradiometer with Known Velocity, in *Detection Technologies for Mines and Minelike Targets*, Dubey, A.C., Cindrich I., Ralston, M. and Rigans, K. (eds.), the International Society for Optical Engineering, pp. 357-367, April 1995.
 8. The Jet Propulsion Laboratory, 4800 Oak Grove Dr., Pasadena, CA 91109.
 9. M.G. Bello, "Hierarchical Multilayer Perception Network Based Fusion Algorithm for Detection/Classification of Mines using Multiple Acoustic Images and Magnetic Data," in *Detection and Redemption Technologies for Mines and Minelike Targets*, A.C. Dubey, R.L. Banard. C.J. Lowe, and J.E. McFee, Eds., the International Society for Optical Engineering, Proc. SPIE 2765, 1996, pp. 84-109, April 1996.
 10. L. Smedley and G. J. Dobeck, "Automated sensor fusion for synthetic aperture sonar and magnetic gradiometer data," CSS TR-96/10, Coastal Systems Station, 1996.
 11. The IBM Corp. Research Division, T. J. Watson Research Center, P.O. Box 218, Yorktown Heights NY 10598.
 12. Ball Aerospace Systems Division, P.O. Box 1062, Boulder, CO 80306-1062.
 13. The Lockheed-Martin Federal Systems (formally Loral Federal Systems Company and the IBM Federal Systems Company), 9500 Godwin Drive, Manassas, VA 22110.
 14. Quantum Magnetics, 7740 Kenamar Court, San Diego, CA 92121-2425.
 15. Naval Research Laboratory, 4555 Overlook Ave., SE., Washington, D.C. 20375-5000.
 16. R.H. Koch, J.R. Rozen, P. Woltgens, T. Picunko, W.J. Goss, D. Gambrel, D. Lathrop, D. Overway and R.F. Wiegert, "High Performance SQUID Feedback Electronics." Rev. Sci. Instrum., vol. 67(8), pp. 2968-2976, 1996.
 17. J.H. Eraker, "Sensor Temperature stability performance of the Advanced Liquid Helium Dewar," in *Advances in Cryogenic Engineering*, vol. 41, in press.
 18. J. Eraker, "Cryogenic nitrogen cooling systems for a deployed high temperature superconducting magnetic gradiometer system," submitted for publication in IEEE Trans. Appl. Sup., August 1996.
 19. R. Cantor, L.P. Lee, M. Teepe, V. Vinetskiy, and J. Longo, "Low Noise, Single-Layer $\text{YBa}_2\text{Cu}_3\text{O}_{7-x}$ DC SQUID Magnetometers at 77K." IEEE Trans. Appl. Sup., vol. 5(2), pp. 2927-2930, 1995.
 20. J.M. Schmidt, L.P. Lee, A. Mathai, A. Matlashov, M. Teepe, V. Vinetskiy, and R. Cantor, "Low-noise YBCO DC SQUID magnetometers for shielded and unshielded operation," unpublished.
 21. J.W. Purpura, T.R. Clem, and R.F. Wiegert, "Nonlinear response in thin film magnetometer sense loops at 77K," IEEE Trans. Appl. Sup., vol. 5(1), pp. 3123-3126, 1995.
 22. J.Z. Sun, W. Gallagher, and R.H. Koch "Nonlinear hysteresis in thin film magnetometers," IEEE Trans. Appl. Sup., vol. 3(1), pp. 2022-2025, 1993.
 23. J.W. Purpura and R.F. Wiegert, "Magnetic hysteresis in $\text{YBa}_2\text{Cu}_3\text{O}_{7-\delta}$ magnetometer sense loops" submitted for publication in IEEE Trans. Appl. Sup., August 1996.
 24. R.H. Koch, J.Z. Sun, V. Foglietta, and W.J. Gallagher, "Flux Dam, a method to reduce extra low frequency noise when a superconducting magnetometer is exposed to a magnetic field," Appl. Phys. Lett., vol. 67(5). pp. 709-711, 1995.
 25. J.W. Purpura and J.M. Schmidt, "Evaluation of a three-channel high-temperature superconducting magnetometer system," unpublished.
 26. R.H. Koch, "Gradiometer having a magnetometer which cancels background magnetic field from other magnetometers," U.S. Patent No. 5,122,744, 1992.
 27. R.H. Koch, J.R. Rozen, J.Z. Sun, and W.J. Gallagher, "A three sensor gradiometer," Appl. Phys. Lett., vol. 63(3), pp. 403-405, 1993.
 28. G.I. Allen, R.H. Koch, and G. Keefe. "Unique man-portable 5 element fluxgate gradiometer system," in *Detection Technologies for Mines and Minelike Targets*, A.C. Dubey, I. Cindrich, M. Ralston, and K. Rigano, eds., the International Society for Optical Engineering, Proc. SPIE 2496, pp. 384-395, 1995.
 29. R.H. Koch, G.A. Keefe, and G. Allen, "Room temperature three sensor magnetic field gradiometer," Rev. Sci. Instrum. 67(1), pp. 230-235, 1996.

Profiles in Science



Albert M. Bottoms

Albert M. Bottoms is the first incumbent of the Ellis A. Johnson Chair of Mine Warfare at the Naval Postgraduate School, Monterey, California. In that capacity since 1992, he has initiated an ONR-sponsored Symposium Series on Technology and the Mine Problem that has received international acclaim. He also founded and is president of the Mine Warfare Association that is dedicated to education and communication about the "mine problem."

He is a retired member of the Navy's Senior Executive Service since 1990. His career includes assignments as an operations research analyst in the Office of the Chief of Naval Operations and with naval forces afloat, and with policy organization in the Office of Secretary of Defense. He also served as a research and development executive in the Naval Air Systems Command and in the Navy Labora-

tory System at the Naval Underwater Systems Center.

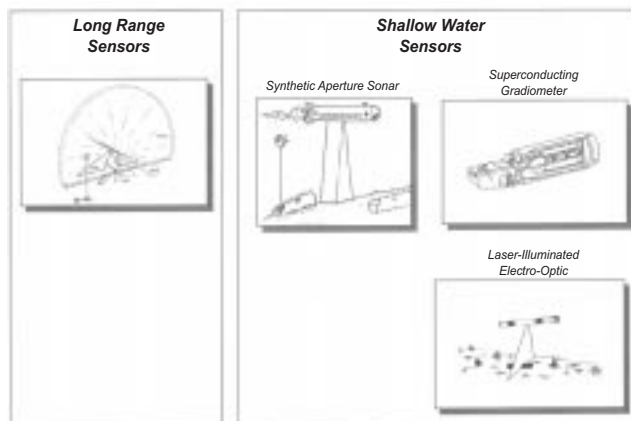
Prior to joining the Federal Service in 1970, Mr. Bottoms was a staff member in the Massachusetts Institute of Technology's Operations Evaluation Group in the Weapons Systems Evaluation Group in the areas of mine warfare and anti-submarine warfare.

Mr. Bottoms has earned degrees from the University of Pennsylvania, Iowa State University, and the Massachusetts Institute of Technology. His activities have been recognized by the Distinguished Service Award (President, Naval War College), The Commander's Award for Meritorious Service (Commander, Defense Systems Management College) and, in May, 1997, by the Department of Navy Medal for Meritorious Public Service (conferred by the Superintendent of the Naval Postgraduate School).

Research Notes

The following are several of the major efforts the Navy is supporting which address the key priorities for mine countermeasures:

Advanced Sensors for Unmanned Undersea and Airborne Vehicles



Program develops technologies for remote reconnaissance capabilities including high-resolution synthetic aperture sonar, electro-optical, and high critical temperature superconducting gradiometer sensors.

Littoral Remote Sensing

A program that will fuse the relevant data available from National sensors and standoff tactical sensor systems to provide the on-scene commander with geomorphologic/environmental and mine/mine field location information.

Shallow Water Airborne Mine Reconnaissance System

A LIDAR system, a derivative of the "Magic Lantern" system, with improved bottom tracking, higher power and spatial resolution

Alternative Detection, Classification, and Localization

Development of new detection and classification approaches using prototype neural network technology.

Explosive Ordnance Disposal

High resolution, hand held, imaging sonar systems for improved mine classification and identification capabilities, support to special warfare and explosive ordnance disposal.

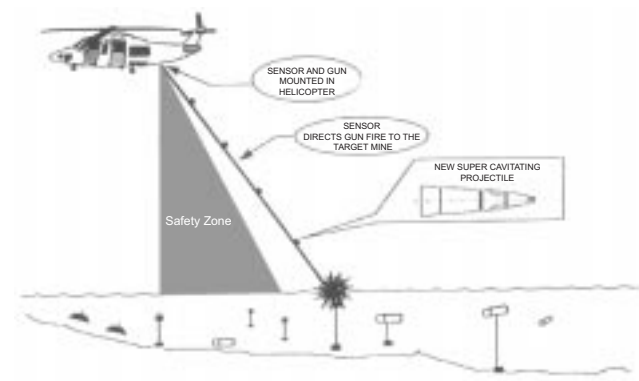
High Search Rate Sonar System

A program to develop advanced sonar and signal processing technology for integration into unmanned undersea vehicles, including enhanced swath width toroidal volume search sonar, advanced side-looking sonar, and computer aided classification techniques.

Advanced Degaussing Technology

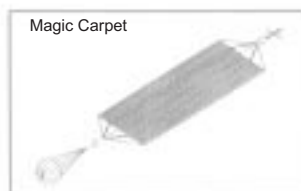
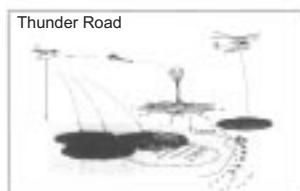
An effort aimed at significantly reducing steel-hull surface ship vulnerability to magnetic mines; focussing on closed loop systems and targeting new construction ships.

Rapid Airborne Mine Clearance System Technology Demonstration



Develop and demonstrate the capability to rapidly target and destroy mines in deep and shallow water from an airborne platform using supercavitating projectiles and targeting LIDAR.

Explosive Neutralization and Obstacle Clearance



Efforts investigating technologies utilizing explosive nets, shaped charges, and explosively formed projectiles; deployment techniques, analytical performance prediction models and simulations are also developed.

Improved Mechanical Mine Sweeping

Advanced bottom contour following capability for sweeping close-moored mines.

Environmental Support

Critical to all aspects of mine countermeasures technology development is an extensive knowledge of the environmental parameters that impact the performance of systems for detection, classification, and clearance of mines and obstacles. The efforts supported here include studies in atmosphere, ocean, ocean bottom and subbottom. Numerical predictive models and environmentally sensitive and adaptive signal processing techniques are also supported. These lead to realistic simulation and training aids.

Near-Term Mine Reconnaissance System

A submarine launched unmanned undersea vehicle that will search for minelike objects and minefields clandestinely.

Advanced Lightweight Influence Sweep System

A system to provide broad and narrow band acoustic and magnetic energy sweep capability; using novel spark-gap and superconducting technology sources to emulate ship signatures.